

A constitutive framework for tension–compression failure asymmetry in soft materials

Yogesh C. Chandrashekar, Kshitiz Upadhyay*

Department of Aerospace Engineering and Mechanics, University of Minnesota, Minneapolis, MN 55455, USA

Abstract

Soft materials often exhibit pronounced tension–compression asymmetry (TCA) in their softening and failure behavior, a feature that conventional hyperelastic and continuum-damage formulations fail to capture within a unified framework. This work presents a Lode-invariant-based hyperelastic softening model that explicitly incorporates deformation-mode dependence through a bi-failure construction with distinct tensile and compressive energy limiters. The proposed model extends Volokh’s classical energy-limiting approach by embedding a Lode-angle-dependent weighting function, which ensures a smooth and thermodynamically consistent transition of failure behavior across distortion modes, achieved directly within the constitutive description of the bulk response—without introducing internal damage variables. Agarose hydrogels (1, 2, and 3% w/v) serve as the model system for validation. The framework accurately reproduces experimental stress–stretch responses in uniaxial tension and compression, capturing concentration-dependent stiffness and failure energetics. Using parameters calibrated solely from combined uniaxial data, the model successfully predicts pure shear behavior—including softening and failure—demonstrating strong cross-mode generalizability. To further assess thermodynamic stability and deformation-mode sensitivity, the model’s energy landscape was analyzed across the full Lode-invariant space, confirming its consistent and stable behavior under diverse loading conditions. Parameter evolution with concentration follows power-law scaling, enabling interpolation and predictive validation at intermediate concentrations (evaluated at 2.5% w/v). By establishing a physically interpretable damage modeling framework over the Lode invariant space, this work provides a unified framework for tension–compression–asymmetric softening and lays the foundation for distortional-mode-sensitive, three-dimensional failure mapping of soft materials.

Keywords: Hyperelasticity, constitutive modeling, soft materials, damage, energy limiters, distortional-mode-dependence

1. Introduction

Soft materials, such as biological tissues, gels, and foams, exhibit complex mechanical behavior characterized by large deformations, nonlinear stress–strain response, gradual damage accumulation, and a pronounced loading-mode based asymmetry between tension and compression, known as tension–compression asymmetry (TCA) [1, 2, 3, 4, 5, 6, 7, 8, 9, 10, 11, 12]. Beyond their elastic characteristics, the inelastic mechanisms governing softening and failure differ fundamentally between deformation modes: under compression, these materials are prone to local buckling and wrinkling [13, 14, 15, 16, 17], whereas tensile loading promotes microcrack formation driven by the collective rupture of molecular bonds at weak cross-links [18, 19, 20, 21]. Despite this well-documented mechanical asymmetry, continuum frameworks capable of accurately capturing such failure-related irreversible phenomena in soft materials remain underdeveloped [22, 23]. This gap is particularly consequential for biomedical applications, where accurate modeling of tissue softening and rupture—such as in brain, vascular, and organ injury—is essential for understanding, diagnosing, and mitigating conditions including stroke, cerebral hemorrhage, and traumatic brain injury [24, 25, 26, 27, 28].

Hyperelasticity provides the fundamental constitutive framework for describing the nonlinear elastic response of soft materials [29, 30, 31, 32]. Classical formulations such as Neo-Hookean, Mooney–Rivlin [33, 34, 35, 36], Ogden [37], along with their variants [38, 3], remain widely adopted because of their

*Corresponding author. Email: kshitizu@umn.edu

tractable strain energy functions, conveniently expressed in terms of principal strain invariants or principal stretches, and their ability to represent large deformations. Nevertheless, their predictive capability is often limited to moderate loading regimes and lacks the ability to capture failure or rupture behavior [39, 40, 41]. Consequently, recent efforts have focused on integrating failure theories into hyperelastic frameworks, yielding constitutive descriptions that capture damage and rupture while retaining computational efficiency [42, 41, 43, 44]. Such extensions are pivotal for advancing the design and analysis of soft materials in both engineering and biomedical applications.

To place these developments in context, it is useful to distinguish between the two primary forms through which damage manifests in soft materials: continuous and discontinuous softening [22, 45, 23]. Continuous softening occurs under large stretches as a gradual reduction in stiffness along the primary loading path, ultimately leading to failure through micro-crack nucleation and growth [46, 45, 22, 47, 48]. In contrast, discontinuous softening appears upon unloading and is associated with the Mullins effect [49, 50, 51], hysteresis, and permanent set—manifested as residual strains after unloading [52, 53, 54, 44].

Among the various damage formulations proposed, the Ogden–Roxburgh pseudo-elastic framework [55] remains widely used to model discontinuous softening via a stress-softening function defined in terms of the maximum strain energy attained. However, this function is activated only upon unloading [56] and thus neglects softening associated with the primary loading path and the ensuing failure [57, 45, 56]. Continuous softening, on the other hand, is most naturally addressed within the continuum damage mechanics (CDM) paradigm, originally rooted in the phenomenological frameworks developed by Kachanov [58] and Rabotnov [59]. CDM employs internal damage variables to progressively degrade the intact strain-energy function—an approach first devised for small-strain isotropic damage [60] and later extended to finite-strain kinematics [61, 62].

While CDM effectively describes softening behavior, the damage variable lacks a direct physical interpretation, as it is an internal thermodynamic state variable [63, 64, 41]. Moreover, as noted by Weisbecker et al. [65] and Anssari-Benam et al. [52, 42], CDM formulations intrinsically couple elastic parameters with the damage variable, hindering independent characterization of the intrinsic material response and complicating experimental calibration. These limitations, along with difficulties in reproducing large-strain responses, have motivated the development of alternative, more physically grounded frameworks for modeling damage in soft solids.

Alternative approaches embed material-dependent damage mechanisms at the microstructural or bond level within continuum formulations. Representative examples from the fibrous tissue literature include: (i) fibril-sliding models—capturing irreversible proteoglycan-bridge sliding across collagen fibrils (Schmidt et al. [66]; Gasser and Miller [67, 68]); (ii) fibril chain-breakage models incorporating stochastic-structurally based damage [69, 70, 71]; and (iii) formulations that incorporate the effects of collagen cross-links in addition to sliding [72], providing a qualitative description of rupture in collagenous soft tissues. While these models are rooted in physical mechanisms and yield valuable mechanistic insight, they typically require fibril-scale information that is difficult to obtain and become computationally demanding when applied to macroscopic problems [22, 73]. Moreover, their material- and architecture-specific assumptions restrict general applicability [74, 75, 76, 77].

To address these limitations, Gao and Klein [78, 79] proposed the more general Virtual Internal Bond (VIB) model, which bridges atomistic and continuum scales by idealizing materials as networks of atoms interconnected by cohesive bonds. Unlike conventional cohesive zone models, which treat fracture and elasticity as separate phenomena through distinct cohesive surface and bulk elements, the VIB framework unifies both elastic and fracture behavior within a single continuum description. This is achieved by incorporating atomic bond potentials into the constitutive response via the Cauchy–Born rule [80, 81], thereby establishing a rigorous atomistic–continuum connection [82, 83, 84, 85, 86, 87]. The VIB framework has been widely employed to capture the nucleation and propagation of cracks in various classes of materials [78, 88, 89, 90, 91], and implemented in finite element (FE) frameworks (e.g., via UMAT in ABAQUS) to reproduce material softening and failure [92]. However, the inherent softening behavior in the VIB formulation often induces numerical instabilities due to strain localization and loss of ellipticity, leading to convergence issues and singular stiffness matrices [92, 91]. Ensuring stability typically requires restrictive measures—such as locally stiffened elements or predefined crack paths [92]—which limit its predictive flexibility. Thus, despite its strong physical foundation, the VIB approach remains computationally demanding and less flexible, motivating the pursuit of more efficient continuum-level, energy-based formulations [84, 91].

As a macroscopic alternative to continuum–atomistic approaches, Volokh et al. [93, 41, 43] introduced a physically motivated phenomenological framework that describes damage-induced softening through energy limiters embedded directly within the hyperelastic constitutive formulation. When coupled with

the material sink concept [19, 94, 95] to account for failure propagation, this framework offers a physically interpretable and computationally efficient alternative to conventional CDM. It eliminates the need for ad hoc damage thresholds or evolution laws typically invoked in CDM, thereby establishing a new paradigm for modeling damage and failure in soft materials. The energy limiters framework has since been integrated with various hyperelastic formulations to capture bulk failure in a wide range of soft materials and biological tissues, as extensively reported in the literature [96, 97, 98, 99, 100, 46, 101, 102, 103, 104].

Despite the advances achieved in prior studies, conventional softening hyperelasticity and related frameworks fail to capture a critical aspect of soft solids: distortion-mode-dependent asymmetry, particularly TCA. In the context of hyperelasticity with energy limiters, this limitation arises from the use of a single set of energy limiting parameters (Φ , m) within the stress-softening formulation, which constrains the model’s ability to differentiate between tensile and compressive responses. Consequently, most existing models are calibrated exclusively using uniaxial tension data, and their predictive capability under different distortion modes or complex multi-loading conditions remains limited [42, 103]. This restricted treatment of TCA is not unique to damage models—it also persists in purely hyperelastic formulations—highlighting a fundamental gap in current constitutive descriptions of soft materials.

The significance of TCA is well established through numerous experimental studies. Normand et al. [105] demonstrated that agarose hydrogels exhibit substantially different elastic moduli, failure stresses, and failure strains in tension and compression. Similar asymmetric responses were reported in ballistic gelatin by Pasumarthy and Tippur [106], and in gellan gels by Tang et al. [107]. Notbohm et al. [20] further emphasized the pivotal role of TCA in biological networks, linking compressive stiffness loss and fibrin microbuckling to cellular mechanosensing in fibrous matrices. More recently, Voyiadjis et al. [108] and Zhu et al. [26] showed that variations in compressibility between tension and compression significantly contribute to TCA, highlighting the necessity of simultaneously accounting for both asymmetry and volumetric effects in constitutive descriptions of brain-tissue mechanics. Together, these studies reveal that both the intrinsic hyperelastic response and the damage tolerance of soft materials are fundamentally asymmetric between tension and compression [109, 16, 3]. Building on this foundation, Latorre et al. [110] theoretically demonstrated that, within the Valanis–Landel [111, 112] framework, complete characterization of incompressible hyperelastic materials requires incorporating both tensile and compressive branches from uniaxial tests. Consistent with this, subsequent investigations showed that material parameters calibrated using only one deformation mode lead to poor predictive capability under multiaxial or combined loading conditions [113, 114, 115, 116]. Collectively, this body of evidence establishes TCA as a defining characteristic of soft solids and exposes a central limitation of current constitutive frameworks—their inability to represent distortion-mode-dependent asymmetry—thereby restricting predictive accuracy under complex loading states.

Progress has been made toward extending hyperelastic formulations to capture TCA in the elastic regime. Among these, the Ogden model can implicitly represent asymmetry through the coefficients α_i [37, 2, 7, 108, 31, 117, 118], which simultaneously govern the degree of nonlinearity in the stress–strain response and the extent of tension–compression disparity. While this offers some flexibility, independent control over these two features is not possible [7]. To overcome this limitation, Du et al. [15, 14] extended Ambartsumyan’s classical bi-modulus concept [119] to a hyperelastic framework by introducing distinct shear moduli for tension and compression based on principal stretches. This approach provides a physically intuitive representation of TCA in the purely elastic regime. However, its applicability remains confined to intact (i.e., undamaged) hyperelasticity—specifically, to separable Valanis–Landel-type formulations (e.g., Neo-Hookean, Ogden) [111, 109]—and therefore cannot account for asymmetry arising from irreversible phenomena such as stress softening or failure.

This limitation highlights a broader gap: while progress has been made in representing elastic asymmetry, extending these principles to the inelastic regime has proven challenging. TCA accompanying damage and failure remains poorly captured within existing hyperelastic-softening or failure frameworks. Moreover, the absence of an explicit energy potential that distinguishes between different distortion modes hinders the formulation of bounding relations capable of rigorously separating tensile and compressive energy contributions at finite strains. Table 1 presents a concise overview of existing damage models and their limitations in the context of the present study. While these available approaches successfully reproduce various aspects of softening and fracture, none explicitly encode distortion-mode sensitivity or TCA within a unified, thermodynamically consistent potential. Collectively, these unresolved gaps motivate the generalized framework proposed herein, developed to capture distortion-mode-dependent softening and failure.

Building upon this motivation, we extend Volokh’s classical energy limiters framework [41, 43, 120] by introducing distortional mode-dependent energy limiters formulated in terms of the Lode invariants

Table 1: Summary of representative damage-modeling frameworks for soft materials. Each approach is briefly evaluated in terms of its principal strengths, key limitations, and relevance to tension–compression asymmetry (TCA).

Framework	Key Merits	Principal Limitations
Pseudo-elasticity	Captures unloading hysteresis and stress-softening with simple closed forms; computationally efficient for cyclic tests.	Describes discontinuous softening only; lacks representation of progressive bond-rupture-driven degradation.
Continuum Damage Mechanics (CDM)	General framework for continuous softening; versatile and FE-ready with numerous evolution laws.	Internal damage variable lacks direct physical meaning; coupling between elastic constants and damage complicates calibration; TCA not explicitly encoded.
Microstructural models	Physically interpretable; captures molecular-to-network degradation mechanisms.	Computationally intensive and material-specific; difficult to generalize or upscale.
Virtual Internal Bond (VIB)	Bridges continuum and atomistic scales through cohesive bond potentials; embeds strength and softening.	Calibration complexity; significant computational overhead;
Energy limiters (i.e., energy-limited hyperelasticity)	Physically interpretable via bounded strain energy; avoids ad hoc thresholds; efficiently couples with standard hyperelastic forms.	Conventional forms assume symmetric softening and failure; no explicit distortion-mode sensitivity or tension–compression distinction.

of the Hencky strain. These invariants—particularly the third invariant K_3 (Lode angle)—uniquely characterizes distinct distortion modes [121, 122, 123, 124, 125, 126, 127, 128], thereby providing a natural basis for defining a bi-failure criterion that captures TCA in softening behavior. The proposed extension is integrated with the strain–energy density function of Prasad and Kannan [125], which employs the same invariant framework to introduce distortion-mode-dependent shear moduli and thereby reproduce TCA in the elastic response [127, 125]. Together, these developments establish a unified Lode invariant-based hyperelastic–damage formulation capable of representing asymmetry in both elastic and inelastic regimes.

To evaluate the predictive capability of the proposed framework, we selected agarose hydrogels as a model material due to their widespread use as tissue phantoms in soft-tissue injury studies [129, 130, 87] and their elastomeric behavior under short-time loading [131, 114]. Experimental characterization involved calibrating the model to combined tension–compression responses of agarose gels at 1, 2, and 3% w/v concentrations using full-field Digital Image Correlation (DIC) for enhanced accuracy. The calibrated model was then validated under pure shear loading to assess its predictive capability beyond the training modes. To further examine the framework’s thermodynamic consistency and generalizability, we analyzed its energy landscape across the full Lode-invariant space, providing a comprehensive evaluation of stability across diverse deformation modes. Additionally, the model was applied to an intermediate (2.5%) agarose concentration not used in calibration to explore generalizability across polymer network densities and potential connections to the micromechanical origins of softening and failure [132, 133, 134].

The remainder of the article is organized as follows: Section 2 discusses the concept of energy limiters to model softening-hyperelasticity-based material failure and the continuum framework of Lode-invariants-based hyperelasticity; Section 3 reviews the microstructural origins of asymmetry in deformation-induced softening; Section 4 introduces a novel Lode-invariants-based constitutive damage model and bi-failure criterion; Section 5 details specimen preparation, testing, and calibration procedures; Section 6 validates and benchmarks the model across deformation modes and gel concentrations; and Section 7 concludes with key findings and future directions.

2. Preliminaries: Kinematics, the classical energy limiters approach to modeling soft material failure, and Lode-invariants-based hyperelasticity

2.1. Kinematics

In the framework of finite strain theory, the motion of a continuum body is described by a bijective mapping χ , which assigns to each material point \mathbf{X} in the reference configuration its spatial position \mathbf{x} in the current configuration at time t as follows [135]:

$$\mathbf{x} = \chi(\mathbf{X}, t). \quad (1)$$

The displacement vector field \mathbf{u} characterizing the motion is consequently defined as

$$\mathbf{u}(\mathbf{X}, t) = \mathbf{x}(\mathbf{X}, t) - \mathbf{X}. \quad (2)$$

A fundamental kinematic quantity is the deformation gradient tensor \mathbf{F} , a two-point tensor that describes the local transformation of material line elements from the reference configuration to the current configuration, given as [135]

$$\mathbf{F}(\mathbf{X}, t) = \frac{\partial \boldsymbol{\chi}(\mathbf{X}, t)}{\partial \mathbf{X}} = \nabla_{\mathbf{X}} \mathbf{x}. \quad (3)$$

Consistent with experimental observations in soft materials [136, 137, 138, 139], we adopt the incompressibility constraint $J = \det \mathbf{F}(\mathbf{X}, t) = 1$.

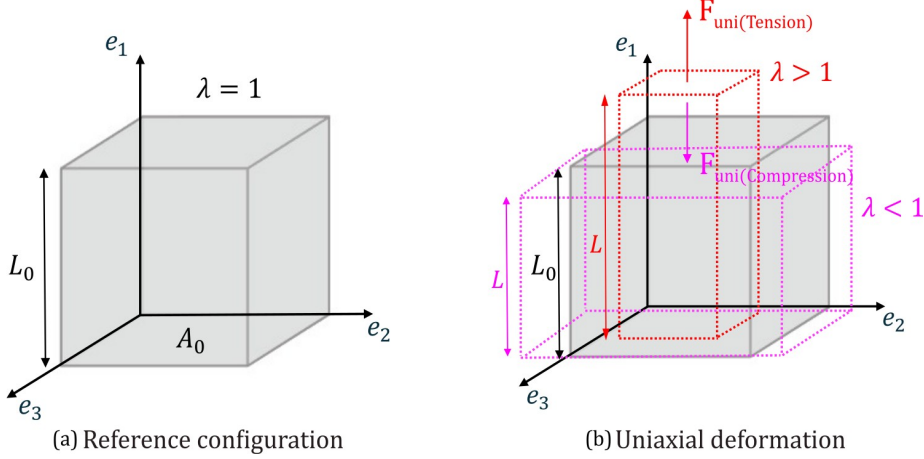


Figure 1: Unit cube in the (a) reference configuration and (b) under uniaxial deformation. Tension ($\lambda > 1$) is shown in red; compression ($0 < \lambda < 1$) in magenta.

Throughout this paper, we use uniaxial and pure shear deformation modes for calibration and/or validation.

- **Uniaxial deformation (compression and tension):** Figure 1 illustrates the uniaxial deformation of a unit cube. $\{\mathbf{e}_1, \mathbf{e}_2, \mathbf{e}_3\}$ denote the orthonormal basis and $\{\lambda_1, \lambda_2, \lambda_3\}$ the corresponding principal stretches. Owing to the incompressibility constraint,

$$\det \mathbf{F} = \lambda_1 \lambda_2 \lambda_3 = 1. \quad (4)$$

For axial loading along \mathbf{e}_1 , the stretch λ_1 becomes

$$\lambda_1 = \lambda = \frac{L}{L_0}, \quad (5)$$

with initial and current gauge lengths L_0 and L , respectively. Under Eq. (4), the associated principal stretches are $\{\lambda, \lambda^{-1/2}, \lambda^{-1/2}\}$, giving the point-wise mapping

$$x_1 = \lambda X_1, \quad x_2 = \lambda^{-1/2} X_2, \quad x_3 = \lambda^{-1/2} X_3, \quad (6)$$

and the deformation gradient

$$\mathbf{F}_{\text{uni}} = \begin{bmatrix} \lambda & 0 & 0 \\ 0 & \lambda^{-1/2} & 0 \\ 0 & 0 & \lambda^{-1/2} \end{bmatrix}. \quad (7)$$

- **Pure shear deformation:** In the classical pure shear geometry (Rivlin–Thomas [140]), illustrated in Fig. 2, a nearly homogeneous state is obtained when the specimen width W far exceeds the gauge height H ($W \gg H$) and the loading is applied parallel to H . Considering a strictly incompressible material, the deformation gradient in pure shear is then expressed using principal stretches $\{\lambda, 1, \lambda^{-1}\}$ with λ stretch along the loading direction \mathbf{e}_1 , yielding

$$x_1 = \lambda X_1, \quad x_2 = X_2, \quad x_3 = \lambda^{-1} X_3 \quad (8)$$

and the deformation gradient

$$\mathbf{F}_{\text{ps}} = \begin{bmatrix} \lambda & 0 & 0 \\ 0 & 1 & 0 \\ 0 & 0 & \lambda^{-1} \end{bmatrix}. \quad (9)$$

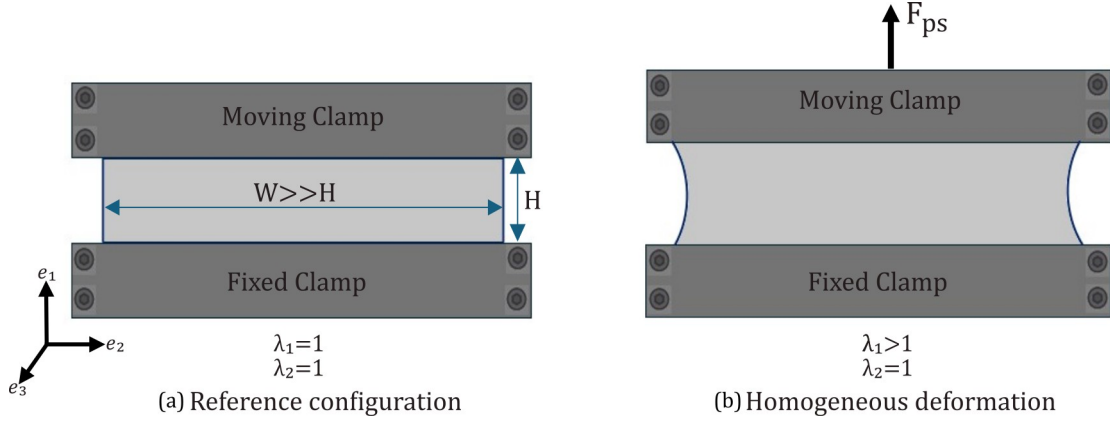


Figure 2: Schematic illustration of a pure shear loading setup in the (a) reference configuration and (b) under homogeneous deformation.

With the uniaxial and pure shear mappings established in Eqs. (7) and (9), we next describe the classical energy limiters approach to modeling damage and failure in soft materials, whose inability to capture TCA formed a major motivation for this work.

2.2. Classical energy limiters approach for modeling continuous softening

The constitutive response of a hyperelastic solid is specified through its strain energy density function $W(\mathbf{F})$, which represents the stored energy per unit reference volume. A fundamental property of conventional hyperelasticity is that W grows indefinitely with increasing deformation, i.e.,

$$\mathbf{F} \rightarrow \infty \Rightarrow W \rightarrow \infty. \quad (10)$$

While mathematically convenient, this result is physically unrealistic as it implies that materials can sustain infinite deformation without failure, contradicting the empirical reality of finite energy storage and damage accumulation in any material.

To overcome this limitation and capture the onset of damage and bulk failure in soft materials, Volokh et al. [96, 41, 93, 141, 142] introduced the concept of energy limiters. This approach imposes a physically motivated upper bound on the strain energy density by introducing material-specific failure parameters (i.e., energy limiters) that capture the maximum energy an infinitesimal material volume can hold before failing. To this end, a bounded, modified strain energy density function ψ was introduced [143] as given below:

$$\text{Volokh damage model: } \psi(W(\mathbf{F})) = \psi_f - \psi_e(W(\mathbf{F})) = \frac{\Phi}{m} \left\{ \Gamma\left(\frac{1}{m}, 0\right) - \Gamma\left(\frac{1}{m}, \left(\frac{W(\mathbf{F})}{\Phi}\right)^m\right) \right\}, \quad (11)$$

where

$$\Gamma(s, x) = \int_x^\infty t^{s-1} \exp(-t) dt \quad (12)$$

is the upper incomplete gamma function. Here, ψ_f is the saturation energy and ψ_e is the recoverable elastic energy. W is the strain energy density in the undamaged material. The modified strain energy density function ψ captures continuous softening and failure via the essential failure condition:

$$\mathbf{F} \rightarrow \infty \Rightarrow \psi(W(\mathbf{F})) \rightarrow \psi_f = \frac{\Phi}{m} \Gamma\left(\frac{1}{m}, 0\right). \quad (13)$$

The softening response is thus governed by two physically interpretable parameters: the pseudo-failure energy Φ that captures the onset of failure in the material (for $m = 1$, $\psi_f = \Phi$), and the softening sharpness parameter m , which controls the sharpness of the transition to instability in the stress-strain response as softening progresses. Note, the model reduces to the conventional intact hyperelastic formulation (i.e., W) as $\Phi \rightarrow \infty$.

By frame indifference and assuming an isotropic response, W of an intact, undamaged material can be written as a function of invariants of any coaxial/isomorphic strain measure built from \mathbf{F} . Common examples include the Neo-Hookean and Mooney–Rivlin models [33, 34] that are based on the principal

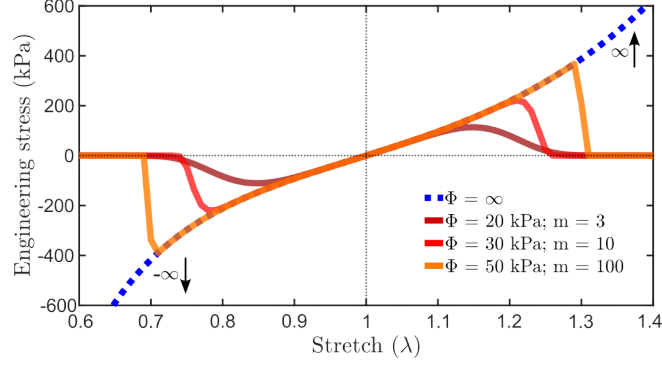


Figure 3: Typical uniaxial engineering stress–stretch responses of the Volokh damage model, considering the one-term Ogden strain energy density to represent intact material behavior. The dashed blue curve shows the undamaged response, while the solid curves demonstrate the softening response for different parameter pairs (Φ, m) , as indicated in the legend. All curves use the following Ogden parameters: $\mu = 300$ kPa and $\alpha = 7$.

invariants (I_1, I_2, I_3) of the right Cauchy–Green tensor $\mathbf{C} = \mathbf{F}^T \mathbf{F}$, and the Ogden model [37] that is based on the principal stretches $(\lambda_1, \lambda_2, \lambda_3)$.

Regardless of the choice of W , the Volokh model always predicts a symmetric uniaxial stress–strain response. To demonstrate this, let’s consider the Ogden hyperelastic model to represent intact behavior in Eq. (11):

$$W_{\text{Ogden}} = \frac{2\mu}{\alpha^2} (\lambda_1^\alpha + \lambda_2^\alpha + \lambda_3^\alpha - 3), \quad (14)$$

where μ is the instantaneous shear modulus and $\alpha \neq 0$ is the nonlinearity parameter. The corresponding principal Cauchy stress components can be obtained as

$$T_i = -p + \lambda_i \frac{\partial \psi}{\partial \lambda_i} \quad (\text{no sum}), \quad (15)$$

where the Lagrange multiplier p imposes incompressibility constraint (Eq. (4)). Under homogeneous uniaxial loading in \mathbf{e}_1 direction (Eq. (7)), we have $\lambda_1 = \lambda$, $\lambda_2 = \lambda_3 = \lambda^{-1/2}$. Accordingly, the partial derivatives in Eq. (15) can be expressed as:

$$\frac{\partial \psi}{\partial \lambda_1} = \frac{\partial \psi}{\partial W} \frac{\partial W}{\partial \lambda_1} = \frac{\partial \psi}{\partial W} \frac{2\mu}{\alpha} \lambda^{\alpha-1}, \quad \frac{\partial \psi}{\partial \lambda_2} = \frac{\partial \psi}{\partial W} \frac{\partial W}{\partial \lambda_2} = \frac{\partial \psi}{\partial W} \frac{2\mu}{\alpha} \lambda^{-\frac{\alpha}{2}-1} \quad (16)$$

Applying the chain rule to Eq. (11) then yields the stress reduction factor, $\text{Red}(\lambda)$, which governs the onset and evolution of softening.

$$\frac{\partial \psi}{\partial W} = \text{Red}(\lambda) = \exp \left[- \left(\frac{W}{\Phi} \right)^m \right]. \quad (17)$$

Using Eqs. (16)–(17) in Eq. (15), and enforcing the traction boundary condition of a nonzero axial stress T_1 with $T_2 = T_3 = 0$, allows determination of the Lagrange multiplier p . Substituting this expression back into Eq. (15) yields the uniaxial Cauchy stress with the energy-limiting (failure) description:

$$\text{Volokh damage model:} \quad T_{\text{Volokh}}^{(\text{uniaxial})} = \exp \left[- \left(\frac{2\mu}{\Phi \alpha^2} (\lambda^\alpha + 2\lambda^{-\alpha/2} - 3) \right)^m \right] \frac{2\mu}{\alpha} (\lambda^\alpha - \lambda^{-\frac{\alpha}{2}}). \quad (18)$$

The corresponding first Piola–Kirchhoff (engineering) stress component, noting that $\mathbf{P} = \mathbf{T}\mathbf{F}^{-T}$, follows:

$$\text{Volokh damage model:} \quad P_{\text{Volokh}}^{(\text{uniaxial})} = \frac{T_{\text{Volokh}}^{(\text{uniaxial})}}{\lambda} = \exp \left[- \left(\frac{2\mu}{\Phi \alpha^2} (\lambda^\alpha + 2\lambda^{-\alpha/2} - 3) \right)^m \right] \frac{2\mu}{\alpha} (\lambda^{\alpha-1} - \lambda^{-(1+\frac{\alpha}{2})}). \quad (19)$$

Figure 3 shows the uniaxial engineering stress–stretch responses predicted using Eq. (19) with Ogden model parameters $\mu = 300$ kPa and $\alpha = 7$ but varying failure parameters Φ and m . The dashed blue curve represents the intact hyperelastic response, while the solid curves illustrate the model’s sensitivity to parameters Φ and m .

A decrease in Φ causes an earlier deviation from the intact curve, signaling premature failure initiation. Conversely, a lower m value reduces the steepness of the post-peak stress decay, leading to a more gradual softening response. A spectrum of failure behaviors—from gradual to abrupt, brittle-like failure (when $m \gg 1$)—can be captured through this model.

From Fig. 3, it is clear that the Volokh damage model enforces a perfectly symmetric tension–compression damage response. This inherent limitation prevents it from capturing the distinct, experimentally observed TCA (and deformation-mode-dependence in general) in continuous softening and failure in soft materials. This limitation forms a key motivation of the present work.

We now describe the concept of Lode invariants and their recent application in deriving strain energy density functions that can efficiently capture TCA in elastic, intact material response.

2.3. Lode-invariants-based hyperelasticity and the Prasad–Kannan model

Capturing the intrinsic TCA in soft materials requires a constitutive framework that can distinguish between different modes of distortion while upholding objectivity and compliance with thermodynamic principles. Classical strain-invariant formulations often fall short in this regard as the conventional invariants of the Cauchy–Green tensor cannot uniquely identify the deformation mode. To address this limitation, we leverage the advantages of a set of orthonormal invariants derived from the logarithmic (Hencky) strain tensor [144, 145], originally introduced by Criscione et al. [121, 146]. These invariants provide a complete and physically interpretable description of isotropic deformation states with mutually orthogonal stress components, wherein the contributions from dilatation and distortion are *a priori* additively separable [147, 148, 122, 149].

Adopting the Hencky strain measure, $\mathbf{E} = \ln \mathbf{V}$, where \mathbf{V} is the left stretch tensor obtained from the polar decomposition $\mathbf{F} = \mathbf{V}\mathbf{R}$ [121, 123, 125], the isotropic Lode invariants are defined as

$$K_1 = \frac{1}{\sqrt{3}} \operatorname{tr}(\ln \mathbf{V}) \quad K_2 = \|\operatorname{dev}(\ln \mathbf{V})\| \quad K_3 = \frac{1}{3} \sin^{-1} \left(\frac{\sqrt{6} \operatorname{tr}[(\operatorname{dev} \ln \mathbf{V})^3]}{\|\operatorname{dev}(\ln \mathbf{V})\|^3} \right) \quad (20)$$

“amount of dilatation” “magnitude of distortion” “mode of distortion”

Each Lode invariant in Eq. (20) possesses distinct physical interpretations [121, 125, 127, 124] as given below:

- $K_1 \in (-\infty, \infty)$ quantifies the extent of volumetric change (dilatation) during deformation. Under the incompressibility constraint (i.e., isochoric conditions), $K_1 = 0$.
- $K_2 \in [0, \infty)$ quantifies the magnitude of distortion.
- $K_3 \in [-\pi/6, \pi/6]$, called the Lode angle, uniquely captures the mode (or type) of distortion. Note, $K_3 = -\pi/6$ for uniaxial compression, $K_3 = 0$ for pure shear, and $K_3 = \pi/6$ for uniaxial tension.

For an isotropic hyperelastic solid, the strain energy density can thus be expressed as a function of the Lode invariants,

$$W = W(K_1, K_2, K_3), \quad (21)$$

which, under incompressibility ($K_1 = 0$), simplifies to

$$W = W(K_2, K_3). \quad (22)$$

Following Criscione et al. [121, 128], the Cauchy stress has an isochoric component associated with the Lagrange multiplier p and a deviatoric component associated with \mathbf{E} , namely

$$\mathbf{T} = -p\mathbf{I} + \frac{\partial W}{\partial \mathbf{E}}. \quad (23)$$

In terms of the Lode invariants of \mathbf{E} , we have

$$\mathbf{T} = -p\mathbf{I} + \frac{\partial W}{\partial K_2} \mathbf{N}_1 + \frac{1}{K_2} \frac{\partial W}{\partial K_3} \mathbf{N}_2, \quad (24)$$

where \mathbf{N}_1 and \mathbf{N}_2 are mutually orthogonal, deviatoric unit tensors associated with distortional magnitude and mode, respectively (explicit forms are provided in Appendix A). The scalar response functions are

$$\gamma_1 = \frac{\partial W}{\partial K_2} = \mathbf{T} : \mathbf{N}_1, \quad \gamma_2 = \frac{1}{K_2} \frac{\partial W}{\partial K_3} = \mathbf{T} : \mathbf{N}_2, \quad (25)$$

where $:$ denotes the double contraction operator, such that $\mathbf{A} : \mathbf{B} = A_{ij}B_{ij}$ for any two second-order tensors \mathbf{A} and \mathbf{B} .

To demonstrate the utility of this Lode-invariants-based framework, we adopt the Prasad–Kannan formulation [125, 127] as the intact hyperelastic potential, originally constructed from brain tissue data to define the first response function. This potential was derived through an *a priori* analysis enforcing the Baker–Ericksen (B–E) inequalities [150] and leveraging the advantages of Lode invariants to ensure thermodynamic admissibility and smooth mode dependence. The strain energy density function of the Prasad–Kannan model is expressed as

$$W_{\text{PK}}(K_2, K_3) = \frac{\mu}{2}K_2^2 + \frac{a[\exp(K_2\mathcal{G}(K_3)) - 1]}{\mathcal{G}(K_3)} - \frac{1}{2}aK_2^2\mathcal{G}(K_3) - aK_2, \quad (26)$$

where $\mu > 0$ is the infinitesimal shear modulus and $a > 0$ is the nonlinear strain-stiffening parameter. The Lode angle-dependent modulus function $\mathcal{G}(K_3)$, derived directly from the B–E inequalities, is given by

$$\mathcal{G}(K_3) = b_0 \left(\frac{\exp\left(\frac{b_1}{2} - b_1 \cos\left(K_3 + \frac{\pi}{6}\right)\right)}{b_1} + \cos\left(K_3 + \frac{\pi}{6}\right) + \frac{1}{6}(\sqrt{7} - 2) \right), \quad (27)$$

with model constants $b_0, b_1 > 0$. This function is positive, smooth, and strictly decreasing from uniaxial compression to tension, ensuring $\gamma_2(K_2, K_3 = \pm\pi/6) = 0$ and thereby maintaining universal uniaxial compatibility.

Substituting Eq. (26) into Eq. (25) yields the first and second response functions of the Prasad–Kannan model as given below [125]:

$$\gamma_{1,\text{PK}} = \frac{\partial W_{\text{PK}}}{\partial K_2} = a(\exp[K_2\mathcal{G}(K_3)] - 1) - aK_2\mathcal{G}(K_3) + \mu K_2, \quad (28)$$

$$\gamma_{2,\text{PK}} = \frac{1}{K_2} \frac{\partial W_{\text{PK}}}{\partial K_3} = - \frac{a(K_2^2\mathcal{G}(K_3)^2 - 2K_2\mathcal{G}(K_3)\exp[K_2\mathcal{G}(K_3)] + 2\exp[K_2\mathcal{G}(K_3)] - 2)\mathcal{G}'(K_3)}{2K_2\mathcal{G}(K_3)^2}. \quad (29)$$

The scalar functions $\gamma_{1,\text{PK}}(K_2, K_3)$ and $\gamma_{2,\text{PK}}(K_2, K_3)$ fully characterize the distortional stress response of the intact material and naturally embed mode dependence through the modulus function $\mathcal{G}(K_3)$. The function $\mathcal{G}(K_3)$ is constructed to monotonically decrease from compression to tension, consistent with experimental observations of human brain tissue reported by Budday et al. [117, 151]. Thus, the Prasad–Kannan model has been shown to capture both bulk and nonlinear shear responses of soft tissues with high fidelity [125], making it an effective baseline model upon which the present damage and failure extension is built.

In summary, the Lode-invariants-based formulation provides a physically interpretable framework that decouples volumetric, distortional, and mode-dependent contributions to deformation. By employing the Prasad–Kannan potential as the intact hyperelastic response, the present study establishes a foundation for extending the energy limiters approach to account for TCA and distortion-mode-dependent softening in a thermodynamically consistent manner. The following section builds upon this formulation to introduce the proposed mode-sensitive failure extension incorporating mode-specific energy limiters. Before presenting this proposed model, we first examine the microstructural origins of TCA in soft material softening and failure.

3. Microstructural Origins of Tension–Compression Asymmetry (TCA) in Soft Material Failure

From a mechanical standpoint, soft materials such as elastomers, hydrogels and biological tissues can be viewed as three-dimensional crosslinked polymer networks capable of sustaining large, finite deformations [6, 152, 153, 154, 155, 156, 157, 158]. Building on this microstructural perspective, the mechanical deformation and progression of damage in fibrous networks under tension can be delineated into three characteristic regimes, each reflecting a distinct stage of hierarchical structural reorganization [159], as outlined below:

1. Regime I (Linear Elastic Response)

At small strains, geometric nonlinearity is minimal, load-bearing fibers respond elastically, and no major network reorientation occurs.

2. Regime II (Microstructural Realignment and Strain Stiffening)

With increasing deformation, fibers progressively align with the loading direction; transversely oriented fibers bend to facilitate the alignment of others. This reorganization introduces pronounced geometric nonlinearity, produces strain stiffening, and is accompanied by notable Poisson contraction.

3. Regime III (Stress-Path Establishment and Failure Onset)

Beyond a critical stretch, nearly straight, aligned chains form continuous load-bearing pathways across the material. As stretch increases, these chains carry growing loads until the weakest crosslink ruptures, marking the transition from distributed microdamage to macroscopic failure.

An analogous three-stage evolution emerges under compression, but with fundamentally different governing processes [160, 161]. The response transitions from an initially linear regime to buckling-dominated softening and ultimately to a densification regime characterized by contact-driven stiffening and energy dissipation.

1. Regime I (Linear Elastic Response)

At small compressive strains, the material exhibits an effective stiffness comparable to that in tension, with negligible network reorganization and minimal fiber deformation.

2. Regime II (Buckling and Softening)

As compressive strain increases, fibers buckle and rearrange, producing a distributed reduction in global load-carrying capacity and a softening response that remains spatially delocalized in random networks.

3. Regime III (Densification and Rapid Stiffening)

At large compressive strains, extensive fiber–fiber contacts form, leading to localized densification, the emergence of crisscrossed bundles, and the activation of frictional and adhesive interactions. These effects collectively produce a sharp increase in stiffness and substantial energy dissipation, thereby governing the material’s capacity for energy absorption under compressive loading.

These processes highlight how the interplay between distortional loading, microstructural evolution, and energy dissipation governs softening and ultimate failure in soft solids. TCA is a defining manifestation of this behavior, reflected in systematically distinct tensile and compressive responses. This asymmetry is particularly pronounced in biological and polymeric soft materials—such as brain tissue, fibrous gels, and elastomeric networks [117, 118, 9]. The distinct mechanisms activated under tension—such as cavitation and microcrack initiation—and under compression—such as fibrillation, crack buckling, and network densification—demonstrate that deformation mode serves as an intrinsic regulator of the mechanical response, including material failure [14, 15, 16, 19, 20, 162, 163]. In biopolymer networks, compressive instabilities commonly originate in weakly connected regions near free surfaces, initially manifesting as surface wrinkles and creases that subsequently propagate into the interior. Such behavior reflects the loss of structural stability in the underlying crosslinked microstructure when subjected to increasing compressive distortion [164, 165, 139, 13]. Collectively, these observations underscore the need for constitutive formulations that explicitly relate failure energetics to the mode of distortion, forming the basis for the generalized Lode-invariant energy-limiting model developed in the subsequent section.

4. A Generalized Framework for Mode-Dependent Failure Using Lode Invariants

The preceding section demonstrated that experimental trends motivate refining the classical energy-limiting form $\psi(W(\mathbf{F})) = \psi_f - \psi_e(W(\mathbf{F}))$ (see Section 2.2, Eqs. (11)–(13)) to account for the TCA observed in softening and rupture.

4.1. Bi-Failure construction with Lode-angle-dependent interpolation

Extending the classical formulation necessitates a mechanism that separates tensile and compressive failure responses while ensuring consistency across all distortional modes. As depicted in Fig. 4, we accomplish this through a *bi-failure construction* that assigns distinct tensile (+) and compressive (−) limiters and introduces mode dependence via the Lode invariants K_2 and K_3 (defined in Section 2.3). The proposed strain energy density ψ_{prop} is given by:

$$\text{Proposed asymmetric failure model: } \psi_{\text{prop}}(W(K_2, K_3)) = \psi_{\text{failure}}^{(\text{prop})}(K_3) - \psi_{\text{elastic}}^{(\text{prop})}(W(K_2, K_3)), \quad (30)$$

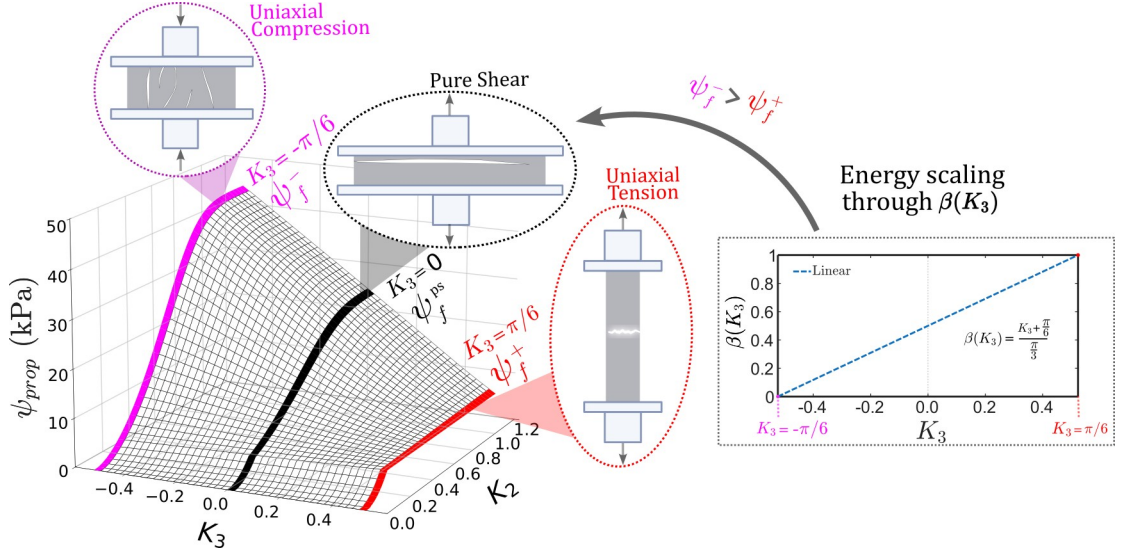


Figure 4: A schematic of the proposed Lode-invariants-based bi-failure framework, with $\psi_{\text{prop}}(W(K_2, K_3))$ as the mode-dependent strain energy density. The colored boundary curves correspond to uniaxial compression ($K_3 = -\pi/6$) (magenta), pure shear ($K_3 = 0$), and uniaxial tension ($K_3 = \pi/6$) (red), with distinct compressive and tensile failure energies ψ_f^- and ψ_f^+ indicated. The inset shows the Lode-weighting function $\beta(K_3)$ that provides a smooth linear interpolation between the compressive ($\beta = 0$) and tensile ($\beta = 1$) branches, enabling a continuous, mode-dependent description of softening and failure across the (K_2, K_3) space and capturing TCA.

where $\psi_{\text{failure}}^{(\text{prop})}$ and $\psi_{\text{elastic}}^{(\text{prop})}$ denote the *mode-dependent failure energy* and *recoverable elastic energy*, respectively, defined as:

$$\text{Proposed failure energy: } \psi_{\text{failure}}^{(\text{prop})}(K_3) = [1 - \beta(K_3)] \psi_f^- + \beta(K_3) \psi_f^+, \quad (31a)$$

$$\text{Proposed elastic energy: } \psi_{\text{elastic}}^{(\text{prop})}(W(K_2, K_3)) = [1 - \beta(K_3)] \psi_e^-(W(K_2, K_3)) + \beta(K_3) \psi_e^+(W(K_2, K_3)). \quad (31b)$$

Here ψ_f^- and ψ_f^+ denote the *compressive* and *tensile* failure energies, respectively. These quantities are *constants* for a given material; in the proposed model, they are defined as (cf. Eq. (13)):

$$\begin{cases} \psi_f^+ = \frac{\Phi^+}{m^+} \Gamma\left(\frac{1}{m^+}, 0\right), \\ \psi_f^- = \frac{\Phi^-}{m^-} \Gamma\left(\frac{1}{m^-}, 0\right), \end{cases} \quad (32)$$

where Φ^\pm and m^\pm are the pseudo-failure energies and softening sharpness parameters, respectively, governing the failure energies under tensile (+; $K_3 = \pi/6$) and compressive (-; $K_3 = -\pi/6$) loading.

In contrast, the quantities $\psi_e^+(W(K_2, K_3))$ and $\psi_e^-(W(K_2, K_3))$ represent the *tension-dominated* (+) and *compression-dominated* (-) recoverable elastic energies, respectively, defined as (cf. Eq. (11)):

$$\begin{cases} \psi_e^+(W(K_2, K_3)) = \frac{\Phi^+}{m^+} \Gamma\left(\frac{1}{m^+}, \left[\frac{W(K_2, K_3)}{\Phi^+}\right]^{m^+}\right), \\ \psi_e^-(W(K_2, K_3)) = \frac{\Phi^-}{m^-} \Gamma\left(\frac{1}{m^-}, \left[\frac{W(K_2, K_3)}{\Phi^-}\right]^{m^-}\right), \end{cases} \quad (33)$$

Although each branch is parameterized by its respective uniaxial energy limiters (i.e., (Φ^+, m^+) or (Φ^-, m^-)), the functions ψ_e^\pm depend on the intact elastic potential $W(K_2, K_3)$ and thus inherit explicit dependence on both Lode invariants (K_2, K_3) . Consequently, ψ_e^+ and ψ_e^- vary smoothly with the distortion mode and quantify the recoverable portion of stored energy available prior to failure for any state characterized by (K_2, K_3) , while ψ_f^\pm define the fixed energetic thresholds identified under the canonical uniaxial modes. For the special cases of uniaxial tension ($K_3 = \pi/6$) and uniaxial compression ($K_3 = -\pi/6$), the corresponding recoverable elastic energies reduce to:

$$\begin{cases} \psi_e^+(W(K_2, K_3 = \frac{\pi}{6})) = \frac{\Phi^+}{m^+} \Gamma\left(\frac{1}{m^+}, \left[\frac{W(K_2, K_3 = \frac{\pi}{6})}{\Phi^+}\right]^{m^+}\right), \\ \psi_e^-(W(K_2, K_3 = -\frac{\pi}{6})) = \frac{\Phi^-}{m^-} \Gamma\left(\frac{1}{m^-}, \left[\frac{W(K_2, K_3 = -\frac{\pi}{6})}{\Phi^-}\right]^{m^-}\right), \end{cases} \quad (34)$$

The $\beta(K_3) \in [0, 1]$ is a continuous Lode-angle-dependent weighting function introduced to ensure a smooth interpolation between the compressive ($\beta(-\pi/6) = 0$) and tensile ($\beta(\pi/6) = 1$) energetic components (Eqs. (32)–(33)). In this study, we adopt a linear weighting function $\beta(K_3)$,

$$\text{Lode-weighting function:} \quad \beta(K_3) = \frac{K_3 + \frac{\pi}{6}}{\frac{\pi}{3}}, \quad K_3 \in \left[-\frac{\pi}{6}, \frac{\pi}{6}\right] \quad (35)$$

Substituting the proposed uniaxial (compression and tension) failure energies and elastic energies (Eqs. (32)–(33)) in Eq. (31), the final expression for the proposed distortion-mode-sensitive strain energy density $\psi_{\text{prop}}(W(K_2, K_3))$ (Eq. (30)) becomes:

$$\begin{aligned} \psi_{\text{prop}}(W(K_2, K_3)) &= \underbrace{\frac{\Phi^-}{m^-} \Gamma\left(\frac{1}{m^-}, 0\right) + \beta(K_3) \left[\frac{\Phi^+}{m^+} \Gamma\left(\frac{1}{m^+}, 0\right) - \frac{\Phi^-}{m^-} \Gamma\left(\frac{1}{m^-}, 0\right) \right]}_{\psi_{\text{failure}}(K_3)} \\ &\quad - \underbrace{\left\{ \frac{\Phi^-}{m^-} \Gamma\left(\frac{1}{m^-}, \left[\frac{W(K_2, K_3)}{\Phi^-}\right]^{m^-}\right) + \beta(K_3) \left[\frac{\Phi^+}{m^+} \Gamma\left(\frac{1}{m^+}, \left[\frac{W(K_2, K_3)}{\Phi^+}\right]^{m^+}\right) - \frac{\Phi^-}{m^-} \Gamma\left(\frac{1}{m^-}, \left[\frac{W(K_2, K_3)}{\Phi^-}\right]^{m^-}\right) \right] \right\}}_{\psi_{\text{elastic}}(W(K_2, K_3))} \end{aligned} \quad (36)$$

The proposed formulation captures deformation-mode-dependent softening and damage evolution as an intrinsic function of the Lode invariants, thereby unifying tension, compression, and intermediate distortional modes within a single thermodynamically admissible framework. Note that following earlier extensions to energy limiters formulations by Volokh et al. [166], irreversibility can be incorporated through a switch parameter ζ implemented via a Heaviside function $H(\zeta)$ to enforce path dependence once the failure threshold is reached. In the present study, however, unloading and healing are not considered; hence, a reversible form is adopted by setting $\zeta = 0$, yielding $H(\zeta) = 1$ (see Appendix B).

In what follows, we derive the Cauchy and engineering stress–stretch relationships for three primary distortion states, establishing a predictive framework for calibration and validation.

4.2. Stress–Stretch relationships for key homogeneous deformation modes

For the proposed softening model $\psi_{\text{prop}}(W(K_2, K_3))$, the Cauchy stress is derived via the chain rule applied to the constitutive relation defined in Eq.(24):

$$\mathbf{T}_{\text{prop}}(W(K_2, K_3)) = -p\mathbf{I} + \frac{\partial \psi_{\text{prop}}}{\partial W} \left(\frac{\partial W}{\partial K_2} \mathbf{N}_1 + \frac{1}{K_2} \frac{\partial W}{\partial K_3} \mathbf{N}_2 \right), \quad (37)$$

Remember, $W(K_2, K_3)$ denotes the strain energy density in the intact/undamaged material. In this study, we adopt the Prasad–Kannan model (Eq. (26)) to represent the intact strain energy density. Thus, the corresponding model response functions, $\frac{\partial W_{\text{PK}}}{\partial K_2} = \gamma_{1,\text{PK}}$ and $\frac{1}{K_2} \frac{\partial W_{\text{PK}}}{\partial K_3} = \gamma_{2,\text{PK}}$ (Eqs. (28)–(29)), capture the intact stress responses which is subsequently modulated within the proposed asymmetric energy-limiting framework.

4.2.1. Uniaxial deformation

Uniaxial deformation is defined kinematically by the principal stretches $\lambda_1 = \lambda$, $\lambda_2 = \lambda_3 = \lambda^{-1/2}$ (Eq. (7)). The corresponding Lode invariants are $K_2 = \frac{\sqrt{3}}{2} |\ln \lambda|$, and $K_3 = \pi/6$ for tension and $K_3 = -\pi/6$ for compression. At these limiting distortion modes, the Lode-weighting function $\beta(K_3)$ attains its boundary values (Eq. (35)), reducing the general potential $\psi_{\text{prop}}(W(K_2, K_3))$ to its mode-specific forms

$$\psi_{\text{prop}}^{(\text{tension})}(W(K_2, K_3 = \frac{\pi}{6})) = \frac{\Phi^+}{m^+} \left[\Gamma\left(\frac{1}{m^+}, 0\right) - \Gamma\left(\frac{1}{m^+}, \left(\frac{W(K_2, K_3 = \frac{\pi}{6})}{\Phi^+}\right)^{m^+}\right) \right], \quad (38)$$

and

$$\psi_{\text{prop}}^{(\text{comp})}(W(K_2, K_3 = -\frac{\pi}{6})) = \frac{\Phi^-}{m^-} \left[\Gamma\left(\frac{1}{m^-}, 0\right) - \Gamma\left(\frac{1}{m^-}, \left(\frac{W(K_2, K_3 = -\frac{\pi}{6})}{\Phi^-}\right)^{m^-}\right) \right]. \quad (39)$$

By employing a universal relation for uniaxial deformation, the second response function vanishes [125], $\gamma_2 = \mathbf{T} : \mathbf{N}_2^{(\text{uniaxial})} = 0$ (see Eq. (25)), implying the stress is governed solely by $\mathbf{N}_1^{(\text{uniaxial})}$. Further, using the spectral decomposition of the Hencky strain $\mathbf{E} = \ln \mathbf{V}$, we have (see [121])

$$\mathbf{N}_1^{(\text{tension})} = \sqrt{\frac{2}{3}} (\mathbf{q}_1 \otimes \mathbf{q}_1 - \frac{1}{2} \mathbf{q}_2 \otimes \mathbf{q}_2 - \frac{1}{2} \mathbf{q}_3 \otimes \mathbf{q}_3), \quad (40a)$$

$$\mathbf{N}_1^{(\text{comp})} = \sqrt{\frac{2}{3}} (-\mathbf{q}_1 \otimes \mathbf{q}_1 + \frac{1}{2} \mathbf{q}_2 \otimes \mathbf{q}_2 + \frac{1}{2} \mathbf{q}_3 \otimes \mathbf{q}_3), \quad (40b)$$

wherein \mathbf{q}_i ($i = 1, 2, 3$) represents the respective principal directions of \mathbf{V} .

With $\mathbf{T} = T_1 \mathbf{q}_1 \otimes \mathbf{q}_1$ under uniaxial loading, enforcing the traction-free lateral boundary conditions ($T_2 = T_3 = 0$) allows determination of the Lagrange multiplier p . For the respective cases of uniaxial tension and compression, this yields:

$$p^{(\text{tension})}(W(K_2, K_3 = \frac{\pi}{6})) = -\frac{1}{\sqrt{6}} \frac{\partial W}{\partial K_2} \frac{\partial \psi_{\text{prop}}}{\partial W} \Big|_{K_3 = \frac{\pi}{6}}, \quad (41a)$$

$$p^{(\text{comp})}(W(K_2, K_3 = -\frac{\pi}{6})) = \frac{1}{\sqrt{6}} \frac{\partial W}{\partial K_2} \frac{\partial \psi_{\text{prop}}}{\partial W} \Big|_{K_3 = -\frac{\pi}{6}}. \quad (41b)$$

Substituting Eqs. (38)–(41) into Eq. (37) yields the Cauchy stress tensors for the corresponding uniaxial deformation modes. The resulting axial Cauchy stress components (T_1) for uniaxial tension and compression are given by:

$$T_{\text{prop}}^{(\text{tension})}(W(K_2, K_3 = \frac{\pi}{6})) = \left(\frac{1}{\sqrt{6}} + \sqrt{\frac{2}{3}} \right) \frac{\partial W}{\partial K_2} \frac{\partial \psi_{\text{prop}}}{\partial W} \Big|_{K_3 = \frac{\pi}{6}}, \quad (42a)$$

$$T_{\text{prop}}^{(\text{comp})}(W(K_2, K_3 = -\frac{\pi}{6})) = -\left(\frac{1}{\sqrt{6}} + \sqrt{\frac{2}{3}} \right) \frac{\partial W}{\partial K_2} \frac{\partial \psi_{\text{prop}}}{\partial W} \Big|_{K_3 = -\frac{\pi}{6}}. \quad (42b)$$

The term $\partial W / \partial K_2$ in the above expressions is from the Prasad-Kannan formulation and is given in Eq. (28).

Since the experimental data are reported as engineering (i.e., first Piola–Kirchhoff) stress–stretch responses, we invoke the standard kinematic relation $\mathbf{P} = \mathbf{T}\mathbf{F}^{-\text{T}}$ to yield the axial components of the first Piola–Kirchhoff stress tensor under tension and compression:

Uniaxial tensile stress (proposed asymmetric failure model):

$$P_{\text{prop}}^{(\text{tension})}(W(K_2, K_3 = \frac{\pi}{6})) = \frac{1}{\lambda} \left(\frac{1}{\sqrt{6}} + \sqrt{\frac{2}{3}} \right) \frac{\partial W}{\partial K_2} \frac{\partial \psi_{\text{prop}}}{\partial W} \Big|_{K_3 = \frac{\pi}{6}}, \quad (43a)$$

$$\text{where } \frac{\partial \psi_{\text{prop}}}{\partial W} \Big|_{K_3 = \frac{\pi}{6}} = \text{Red}_{\text{prop}}^{(\text{tension})}(\lambda) = \exp \left[-\left(\frac{W}{\Phi^+} \right)^{m^+} \right]. \quad (43b)$$

Uniaxial compressive stress (proposed asymmetric failure model):

$$P_{\text{prop}}^{(\text{comp})}(W(K_2, K_3 = -\frac{\pi}{6})) = -\frac{1}{\lambda} \left(\frac{1}{\sqrt{6}} + \sqrt{\frac{2}{3}} \right) \frac{\partial W}{\partial K_2} \frac{\partial \psi_{\text{prop}}}{\partial W} \Big|_{K_3 = -\frac{\pi}{6}}, \quad (43c)$$

$$\text{where } \frac{\partial \psi_{\text{prop}}}{\partial W} \Big|_{K_3 = -\frac{\pi}{6}} = \text{Red}_{\text{prop}}^{(\text{comp})}(\lambda) = \exp \left[-\left(\frac{W}{\Phi^-} \right)^{m^-} \right]. \quad (43d)$$

In Eqs. (43b)–(43d), $\text{Red}_{\text{prop}}^{(\text{ten})}(\lambda)$ and $\text{Red}_{\text{prop}}^{(\text{comp})}(\lambda)$ are mode-dependent *stress-reduction factors* that regulate the transition from the intact elastic state to the damaged (softening) regime under uniaxial tension and compression, respectively (cf. Eq. (17)).

Having established the mode-specific stress–stretch responses under uniaxial deformation, we next generalize the formulation to capture a distinct distortional mode: pure shear.

4.2.2. Pure shear deformation

Pure shear deformation is defined kinematically by the principal stretches: $\lambda_1 = \lambda$, $\lambda_2 = 1$, $\lambda_3 = \lambda^{-1}$ (Eq. (9)). The corresponding Lode invariants are $K_2 = \sqrt{2}|\ln \lambda|$ and $K_3 = 0$. Thus, the Lode-weighting function $\beta(K_3 = 0) = \frac{1}{2}$, indicating that the proposed potential $\psi_{\text{prop}}^{(\text{ps})}$ (Eq. (30)) represents the average of the tensile and compressive distortion modes

$$\begin{aligned} \psi_{\text{prop}}^{(\text{ps})}(W(K_2, K_3 = 0)) = \frac{1}{2} & \left[\frac{\Phi^+}{m^+} \left(\Gamma\left(\frac{1}{m^+}, 0\right) - \Gamma\left(\frac{1}{m^+}, \left[\frac{W(K_2, K_3 = 0)}{\Phi^+}\right]^{m^+}\right) \right) \right. \\ & \left. + \frac{\Phi^-}{m^-} \left(\Gamma\left(\frac{1}{m^-}, 0\right) - \Gamma\left(\frac{1}{m^-}, \left[\frac{W(K_2, K_3 = 0)}{\Phi^-}\right]^{m^-}\right) \right) \right]. \end{aligned} \quad (44)$$

The associated pure-shear-specific failure and elastic energy contributions are obtained as:

$$\text{Failure energy (pure shear):} \quad \psi_f^{(\text{ps})}(K_3 = 0) = \frac{\psi_f^+ + \psi_f^-}{2}, \quad (45a)$$

$$\text{Elastic energy (pure shear):} \quad \psi_e^{(\text{ps})}(W(K_2, K_3 = 0)) = \frac{\psi_e^+(W(K_2, K_3 = 0)) + \psi_e^-(W(K_2, K_3 = 0))}{2}. \quad (45b)$$

Since $K_3 = 0$, the second response function $\gamma_2 = \frac{1}{K_2} \frac{\partial W}{\partial K_3}$ (Eq. (29)) vanishes and the corresponding kinematic tensor $\mathbf{N}_2^{(\text{ps})}$ does not contribute to the Cauchy stress in Eq. (24). The stress response therefore depends exclusively on $\gamma_1 = \frac{\partial W}{\partial K_2}$ (Eq. (28)), with the corresponding unit kinematic tensor [121]:

$$\mathbf{N}_1^{(\text{ps})} = \frac{1}{\sqrt{2}}(\mathbf{q}_1 \otimes \mathbf{q}_1 - \mathbf{q}_3 \otimes \mathbf{q}_3). \quad (46)$$

Under pure shear, $\mathbf{T} = T_1 \mathbf{q}_1 \otimes \mathbf{q}_1 + T_2 \mathbf{q}_2 \otimes \mathbf{q}_2$, and the traction-free condition in the thickness direction ($T_3 = 0$) yields the Lagrange multiplier from the general stress relation (Eq. (37)):

$$p^{(\text{ps})}(W(K_2, K_3 = 0)) = -\frac{1}{\sqrt{2}} \frac{\partial W}{\partial K_2} \frac{\partial \psi_{\text{prop}}}{\partial W} \Big|_{K_3=0}. \quad (47)$$

Substituting Eq. (47) in Eq. (37) yields the Cauchy stress tensor. The axial stress component (T_1) for pure shear deformation is then given by:

$$T_{\text{prop}}^{(\text{ps})}(W(K_2, K_3 = 0)) = \sqrt{2} \frac{\partial W}{\partial K_2} \frac{\partial \psi_{\text{prop}}}{\partial W} \Big|_{K_3=0}. \quad (48)$$

Using $\mathbf{P} = \mathbf{T}\mathbf{F}^{-\text{T}}$, the corresponding axial component of the first Piola–Kirchhoff stress is derived as

Pure shear axial stress (proposed asymmetric failure model):

$$P_{\text{prop}}^{(\text{ps})}(K_2, K_3 = 0) = \frac{T_{\text{prop}}^{(\text{ps})}}{\lambda} = \frac{1}{\sqrt{2}\lambda} \frac{\partial W}{\partial K_2} \frac{\partial \psi_{\text{prop}}}{\partial W} \Big|_{K_3=0}, \quad (49a)$$

$$\text{where } \frac{\partial \psi_{\text{prop}}}{\partial W} \Big|_{K_3=0} = \text{Red}_{\text{prop}}^{(\text{ps})}(\lambda) = \frac{1}{2} \left[\exp \left[-\left(\frac{W}{\Phi^+}\right)^{m^+} \right] + \exp \left[-\left(\frac{W}{\Phi^-}\right)^{m^-} \right] \right]. \quad (49b)$$

Overall, the specific asymmetric failure model proposed in Eq. (36), when employing the Prasad–Kannan formulation [125] (Eqs. (26–29)) as the intact hyperelastic baseline, comprises eight material parameters (see Table 2)—four elastic parameters (μ, a, b_0, b_1) and four mode-specific failure parameters (Φ^\pm, m^\pm). Nevertheless, the generalized bi-failure framework (Eq. (30)) developed in this study remains agnostic to the specific choice of hyperelastic model; any formulation expressed in terms of the Lode invariants is fully compatible with the mode-dependent energy-limiting structure introduced here. Furthermore, once the uniaxial tension and compression responses are used to calibrate the failure parameters, the model provides a complete description of failure across the entire distortion space. Intermediate deformation modes—such as pure shear—are naturally captured through the Lode-weighting function $\beta(K_3)$.

Table 2: Model parameters for the proposed asymmetric failure model in Eq. (36), which is based on a Lode-invariants-based bi-failure formulation. Note, our generalized formulation (Eq. (30)) is agnostic to the choice of the hyperelastic model.

Hyperelastic parameters (Prasad–Kannan model)		
Symbol	Description	Unit
μ	Infinitesimal shear modulus	kPa
a	Nonlinear strain-stiffening parameter	kPa
b_0 b_1	Mode-dependent modulus modulation parameters	–
Mode-specific failure parameters (energy limiters)		
<i>Tension branch (+)</i>		
Φ^+	Tensile pseudo-failure energy parameter	kPa
m^+	Tensile softening sharpness parameter	–
<i>Compression branch (–)</i>		
Φ^-	Compressive pseudo-failure energy parameter	kPa
m^-	Compressive softening sharpness parameter	–

With the constitutive framework and associated stress–deformation relations now established, the following section details the experimental methodology employed to generate the data for model calibration and validation.

5. Model Fitting and Validation Methodology

Calibration of the proposed asymmetric–failure constitutive model requires experimental data that sufficiently span the distortional response of the material—both in magnitude (K_2) and mode (K_3)—to enable independent identification of mode-dependent (tensile and compressive) hyperelastic and failure parameters. Accordingly, both uniaxial tension and compression tests were performed to capture the mode-dependent softening and failure behavior necessary for parameter calibration. The inclusion of both deformation modes is therefore intrinsic to the model formulation, ensuring that the full TCA is represented within the fitted response.

Agarose hydrogels were selected as the model material system due to their well-characterized polymer network structure, elastomeric behavior, and frequent use as soft-tissue phantoms. Three concentrations (1, 2, and 3 % w/v) were investigated to provide a set of related “model materials” that span different network densities. These variations in polymer concentration introduce controlled differences in stiffness, failure strain, and microstructural mechanisms of deformation, thereby allowing evaluation of the framework’s predictive capability across materials with systematically varying architectures.

The overall methodology comprises four stages. First, uniaxial tension and compression experiments were conducted on the three agarose concentrations using standardized specimen preparation, fixturing, and testing protocols, with full-field strain measurement obtained via DIC. The model parameters were calibrated by solving a constrained nonlinear least-squares optimization problem using the combined uniaxial data, ensuring thermodynamic admissibility and avoiding local minima through a multi-start strategy. Second, the calibrated model was validated under pure shear loading to assess predictive generalizability across deformation modes. Third, the energy landscape of the formulation was analyzed across the full K_2 – K_3 invariant space to examine thermodynamic stability and deformation-mode sensitivity beyond the specific loading paths. Finally, the relationship between the calibrated parameters and agarose concentration was characterized using power-law scaling, and the resulting trends were employed to predict the constitutive response of an intermediate, untested concentration (2.5 % w/v) under both uniaxial and pure shear conditions.

This integrated methodology yields a unified, self-consistent framework for evaluating the proposed model’s performance across deformation modes, invariant space, and polymer network densities. The

following subsections detail the experimental procedures for specimen preparation and mechanical testing, followed by the model calibration and fitting process. All corresponding analyses, validation, and discussions of results are presented subsequently in Section 6.

5.1. Sample preparation

Agarose specimens of all three concentrations (1, 2, and 3 % w/v) were prepared using a standardized protocol reported previously in Upadhyay et al. [114, 167]. Briefly, agarose powder (0.15% sulfate; Fisher Scientific, USA) was dispersed in deionized water at the required weight-to-volume ratios and heated in a microwave oven until fully dissolved, with intermittent agitation to ensure optical clarity and homogeneity. Heating duration varies depending on the polymer concentration and total solution volume. Immediately after heating, the solution was weighed and the evaporative water loss was replenished to restore the target concentration. The hot solution was then allowed to rest for 2–5 minutes to release entrapped air bubbles before being cast into custom-designed molds: rubber molds for cylindrical (compression) specimens and 3D-printed nylon carbon fiber molds for dog-bone (tension) and pure shear geometries. All specimens were stored in deionized water to maintain full hydration and were tested within 30 minutes of gelation to minimize evaporative losses and ensure consistent mechanical response.

5.2. Mechanical testing

All mechanical tests, including compression, tension, and pure shear, were performed at ambient room temperature under displacement control using a single-column universal testing machine (Frame 240, TestResources, Inc., Shakopee, MN). A 1.1 kN load cell was used to record force data. All tests were conducted at a quasi-static engineering strain rate of 0.01 s^{-1} using appropriate fixtures for each test configuration, as illustrated in Fig. 5. For each gel concentration, four tests were conducted to ensure reproducibility. The specific configurations corresponding to each deformation mode are described below.

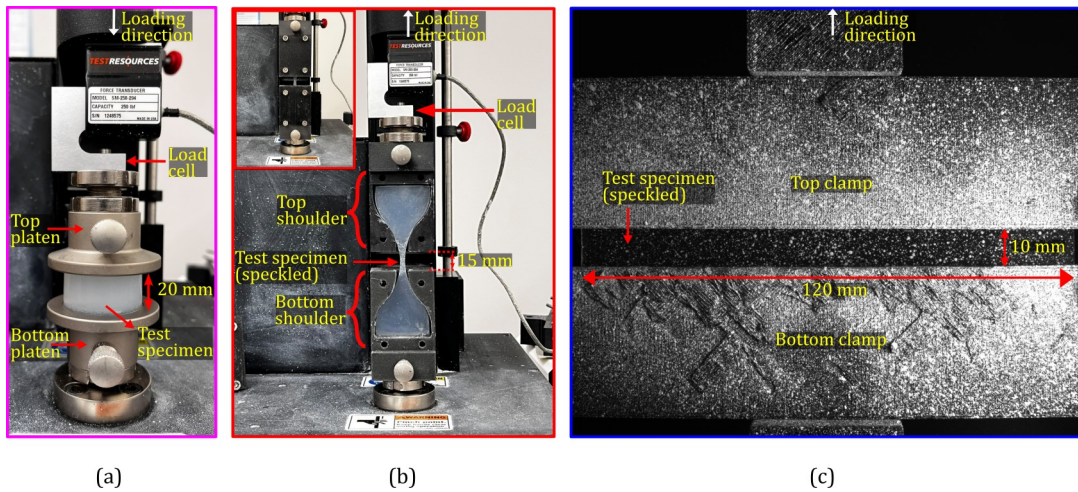


Figure 5: Experimental setup for mechanical testing of agarose gels: (a) uniaxial compression between parallel platens; (b) uniaxial tension of a dog-bone specimen (inset shows the assembled fixture with mounting plates); and (c) pure shear of a rectangular strip clamped between rigid jaws. Prior to loading, a high-contrast speckle pattern was applied on all specimens using white acrylic spray paint to facilitate DIC (excluding compression testing).

5.2.1. Uniaxial compression

Uniaxial compression tests (Fig. 5(a)) were performed on cylindrical agarose specimens with dimensions of 40 mm in diameter and 20 mm in height. Each specimen was placed between two polished steel platens; a thin layer of lubricant was applied to minimize frictional constraint and promote uniform axial deformation. Compression was imposed by translating the top platen downward at 12 mm/min, corresponding to an engineering strain rate of 0.01 s^{-1} . The instantaneous specimen height was computed using the real-time cross-head displacement values. Engineering stress and strain were computed from the load-cell force and platen displacement, respectively, and the test was continued until failure of the specimen.

5.2.2. Uniaxial tension

The uniaxial tension setup, shown in Fig. 5(b), employed a modified dog-bone specimen geometry (from Upadhyay et al. [168]) designed to promote failure within the gauge section while minimizing stress concentrations near the grips. To prevent pre-damage during mounting, the curved shoulders of the specimen were supported using 3D-printed nylon carbon fiber clamps, following the procedure of Wale et al. [169]. The gauge section dimensions were 15 mm (length) \times 4 mm (width) \times 3 mm (thickness). Tensile loading was applied by translating the top shoulder vertically at a constant speed, corresponding to a nominal strain rate of 0.01 s^{-1} , while the bottom shoulder is fixed to the machine base plate. Engineering stress was obtained from load-cell measurements; however, accurate strain determination in such soft, slippery materials requires additional considerations [114, 168], which are discussed in the following paragraph.

Accurate strain measurement in hydrogels during mechanical testing (excluding compression) is challenging due to their extremely compliant nature and low-friction surfaces. Conventional approaches such as crosshead displacement are unsuitable because slippage at the grips introduces substantial errors in estimating accurate material strain [170]. Likewise, contact-based extensometers cannot be employed: even minimal clamping pressure from a clip-on device can induce localized deformation or trigger premature cracking in soft gels [171, 114]. To overcome these limitations, the present study employs DIC—a non-contact optical technique that tracks a randomly distributed speckle pattern on the specimen surface to obtain full-field kinematic measurements. For uniaxial tension, a 3D stereo-DIC configuration was used to capture both in-plane and out-of-plane displacements. Synchronized 5 MP CCD cameras (BFS-U3-51S5M-C, FLIR), positioned at approximately 30° , acquired stereo images at 5 Hz. A set of 30 images of a standard calibration grid was used to perform the stereo-system calibration. The images were processed in MatchID (MatchID, Inc., Belgium) to compute axial engineering strain using a virtual extensometer placed on either side of the damage-initiation region within the gauge section. This approach ensured accurate strain quantification while avoiding artifacts associated with localized edge effects or out-of-plane motion.

This measurement protocol closely follows established procedures for similar soft materials, including PDMS elastomers and agarose hydrogels [168, 114]. These prior studies have extensively validated the assumption of nearly ideal uniaxial deformation within the gauge section, together with the use of material incompressibility ($K_1 = 0$) and isotropy—assumptions that remain well-supported and are not re-evaluated here.

5.2.3. Pure shear

The pure shear configuration (Fig. 5(c)) was implemented by clamping a wide and thin rectangular specimen between rigid jaws to approximate planar tension [172, 173]. The specimen dimensions were 120 mm (width) \times 70 mm (height) \times 2 mm (thickness). Of the total height, 30 mm was clamped on each side, resulting in a gage section of 120 mm \times 10 mm \times 2 mm (see Fig. 5(c)). This gage section geometry was chosen based on established guidelines [174] to minimize edge effects and ensure a uniform strain field. It promotes homogeneous thinning in the thickness direction while suppressing lateral contraction due to Poisson effect, thereby producing a near-pure-shear state in the central region of the specimen (Eq. (9)). Tests were performed under quasi-static loading at a nominal strain rate of 0.01 s^{-1} by vertically translating the top clamp while keeping the bottom clamp fixed to the machine base.

Full-field strain measurements were obtained using 2D DIC with a single 5 MP camera operating at 30 Hz. The spatial resolution was ~ 19 pixels/mm, such that around 190 pixels exist along the height of the specimen gage section. Acquired images were analyzed using the commercial MatchID software; subset size was selected for individual imaging data based on the speckle density and size (subset size $> (3 \times \text{speckle size})$), and also the sigma value (one standard deviation confidence interval) of the subset tracking function. The use of 2D DIC was justified by the negligible out-of-plane deformation of the thin specimens and by maintaining a sufficiently large distance (at least 100 mm) between the camera lens and the specimen surface. Because in-plane strain errors in 2D DIC are approximately proportional to the ratio of out-of-plane displacement to the lens-specimen distance [175], the combination of small specimen thickness (2 mm) and large imaging distance ensures that these errors remain negligible.

Accurate strain quantification in pure shear tests up to the onset of damage localization requires further methodological considerations. Although the full-specimen DIC area of interest (AOI) satisfies the ideal pure shear kinematics, failure in wide-thin agarose specimens can initiate closer to the grip-adjacent regions due to geometric constraints. Consequently, once strain localization develops, spatial averaging of full-field strain becomes increasingly unreliable. To address this issue, the present study

extrapolates the average engineering strain measured during the homogeneous deformation regime (i.e., prior to localization) from full-specimen AOI (average) to the locally measured failure stretch at the rupture-zone. The corresponding engineering stress obtained from the load cell is then mapped to this extrapolated stretch, yielding a consistent and accurate engineering stress–stretch curve for pure shear loading up to failure. [Appendix C](#) details this data analysis procedure and demonstrates that the deformation state achieved in our tests accurately corresponds to the ideal pure shear condition.

5.3. Fitting process

The nominal stress–stretch relations (Eqs. (43a)–(43d)) derived in Section 4 were implemented in MATLAB for parameter identification. For each agarose concentration (1, 2, and 3% w/v), four independent specimens were tested in uniaxial tension and four in uniaxial compression up to failure. To construct representative combined datasets for model calibration, one tension dataset and one compression dataset were randomly paired to form a matched tension–compression set. This procedure was repeated to obtain four distinct combined datasets per concentration, ensuring that each calibration instance reflects independent experimental realizations of both loading modes.

The model parameters were then identified by simultaneously fitting the tension and compression branches of each combined dataset. This was achieved by minimizing an objective function based on the residual sum of squares (RSS), which quantifies the discrepancy between the model predictions and the corresponding experimental measurements.

$$RSS = \sum_{i=1}^k (P_i^{\text{model}} - P_i^{\text{exp}})^2, \quad (50)$$

where k represents the number of experimental data points, P_i^{exp} is the experimentally measured engineering stress at the i th point, and P_i^{model} is the corresponding model-predicted engineering stress.

To ensure robust parameter identification, the fitting procedure begins by specifying initial guesses and bounds for both the hyperelastic and damage-related parameters. A Latin Hypercube Sampling scheme (`lhsdesign`) is employed to generate 500 randomly distributed initial parameter sets, thereby broadening the exploration of the search space and increasing the likelihood of identifying the global minimum. Each initialization is then used to launch a local optimization via `lsqnonlin` within a `MultiStart` framework. The `lsqnonlin` algorithm iteratively updates the parameters to minimize the RSS. Convergence is enforced when either the supremum norm of the objective-function gradient or the Newton step falls below 10^{-6} . The `MultiStart` procedure terminates once all initial points have been processed and the optimal parameter set is selected based on the lowest residual error.

Along with the plots of the fitted responses, the relative errors were computed for each data point to assess the accuracy of the model, using the following expression:

$$\text{err}_i(\%) = \frac{|P_i^{\text{exp}} - P_i^{\text{model}}|}{\max\{0.1 \max(P^{\text{exp}}), |P_i^{\text{exp}}|\}} \times 100, \quad i = 1, 2, \dots, m. \quad (51)$$

The above equation quantifies the relative deviation between the experimental data P^{exp} and the model prediction P^{model} for the i th data point. The term $0.1 \max(P^{\text{exp}})$ is included in the denominator to prevent artificially large relative errors in the small strain regime (when stresses are very small). Expressed as a percentage, this metric provides a consistent measure of model accuracy [176]. Accurate calibration therefore requires the stress–stretch relations derived in Section 4 to closely align with the corresponding experimental uniaxial data. The set of eight unknown model parameters identified through this calibration procedure—four governing the intact hyperelastic response and four describing the mode-specific failure behavior—is summarized in [Table 2](#). The following constraints were enforced during the optimization:

$$\mu > 0, \quad a > 0, \quad b_0 > 0, \quad b_1 > 100, \quad \Phi^+ > 0, \quad m^+ > 0, \quad \Phi^- > 0, \quad m^- > 0.$$

The lower bound on b_1 follows the recommendation in [125].

To assess the robustness and generalizability of the calibrated parameters, the model is subsequently evaluated under an independent distortional loading condition—pure shear. Specifically, the theoretical pure shear predictions given by Eq. (49) are compared directly against experimental test data, thereby confirming the model’s capability to capture multi-mode responses.

With the parameter identification framework established, the next step is to assess the model’s performance against experimental data. The ensuing section presents a detailed comparison between experimental observations and model predictions, followed by a discussion of the calibrated parameters, their physical interpretation, and concentration-dependent trends.

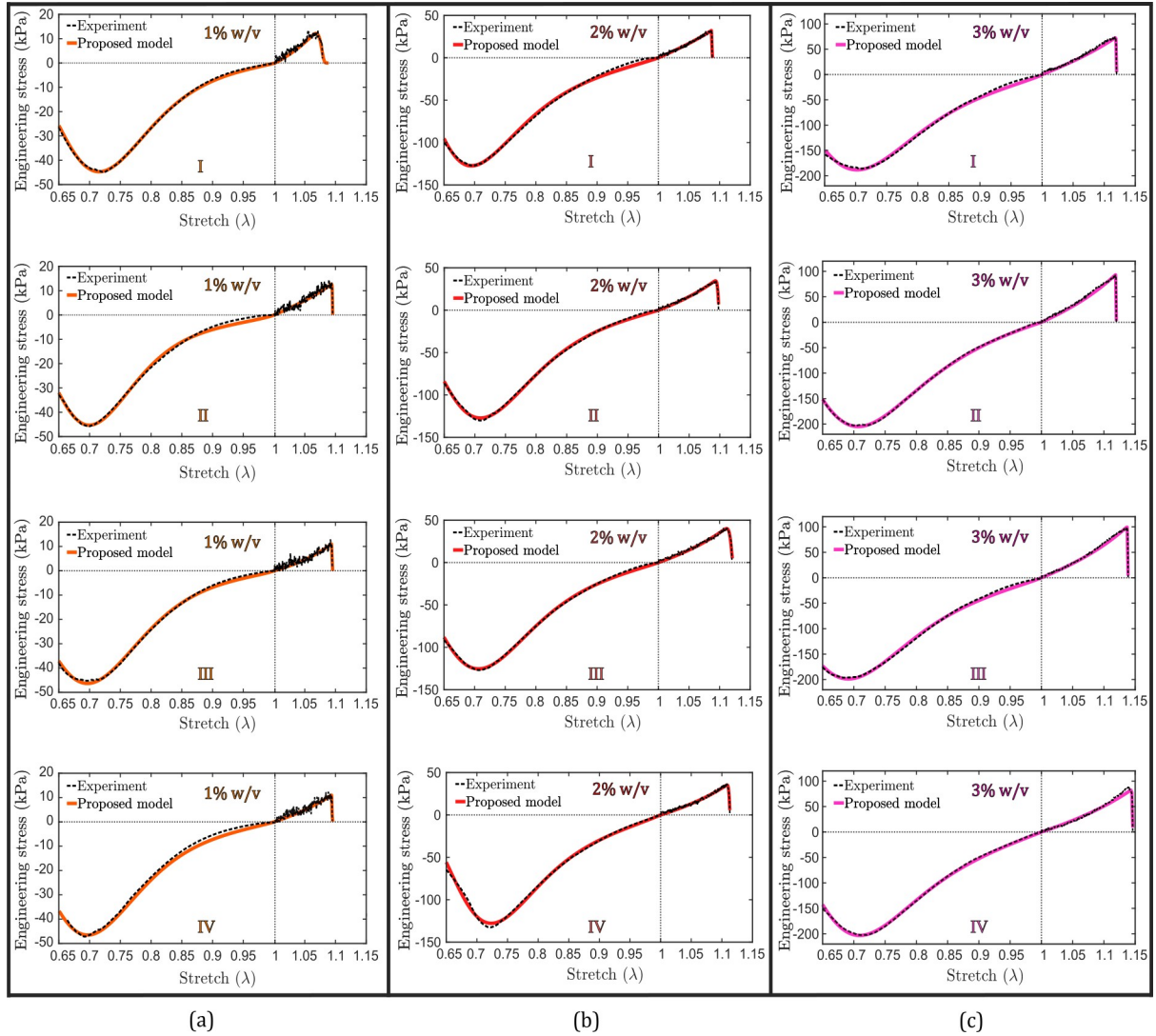


Figure 6: Combined experimental uniaxial engineering stress–stretch data (black) and the corresponding simultaneous fits of the proposed asymmetric-failure model for agarose gels at (a) 1% w/v (orange), (b) 2% w/v (red), and (c) 3% w/v (magenta), shown for each replicate (I–IV). Note: Y-axis scales differ between subplots for clarity.

6. Results and Discussion

6.1. Model calibration and performance under uniaxial deformation modes

The proposed asymmetric-failure constitutive model was calibrated using combined uniaxial tension and compression data obtained from four independent experimental replicates ($n = 4$) for each agarose concentration (1, 2, and 3% w/v). Figure 6 presents the experimental stress–stretch responses (black) and the corresponding model predictions (orange, red, and magenta) for all three concentrations. Each fitting used one random combination of tensile and compressive datasets from the same concentration to ensure robustness of parameter identification. The consistency observed among the replicate measurements (i.e., I–IV) validates the reproducibility of the experimental procedure and supports the assumption of representative material behavior within each concentration group. From the figure, the proposed formulation successfully reproduces the characteristic asymmetric behavior between tension and compression, capturing both softening and failure transitions. The fitted parameters and average residual errors are summarized in Table 3, and the associated total failure energies in Table 4.

Before analyzing the concentration-dependent trends, it is important to interpret the physical roles of the bulk hyperelastic parameters in the Prasad–Kannan formulation (Eq. (26)). The instantaneous shear modulus μ governs the small-strain stiffness and represents the initial linear elastic response of the network. The coefficient a controls the amplitude of the exponential growth of intact strain energy density at large strains (i.e., elastic strain-stiffening behavior) [125, 177]. The constants b_0 and b_1 appear in the mode-dependent modulus function $\mathcal{G}(K_3)$, which governs the degree of TCA and enables the model

Table 3: Model parameters for the proposed asymmetric damage model obtained by fitting combined tension and compression data of agarose gels. The last column reports the overall average residual error of fit for each sample.

sample	μ (kPa)	a (kPa)	b_0	b_1	Φ^+ (kPa)	m^+	Φ^- (kPa)	m^-	$\overline{\text{err}}$ (%)
1% w/v									
I	57.50	1.62	10.15	3867.21	0.52	168.26	0.13	0.22	9.74
II	38.34	3.07	8.53	1116.54	0.42	185.26	0.30	0.24	8.91
III	40.80	2.31	9.08	1120.96	0.43	197.38	0.46	0.26	7.44
IV	62.54	5.89	10.11	350.81	0.52	5.99	0.01	0.17	8.57
<i>Avg.</i>	49.79	3.22	9.47	1613.88	0.47	139.22	0.23	0.22	8.66
2% w/v									
I	156.35	6.05	7.55	3767.95	1.85	43.36	5.45	0.36	7.46
II	187.76	6.60	8.04	2863.50	1.63	33.06	3.31	0.31	8.35
III	174.31	6.65	7.52	4907.38	2.35	22.41	4.68	0.34	8.16
IV	179.06	8.49	7.80	1443.68	1.29	287.34	2.69	0.30	6.99
<i>Avg.</i>	174.37	6.95	7.73	3245.63	1.78	96.54	4.03	0.33	7.74
3% w/v									
I	305.11	15.29	6.35	1827.11	3.98	186.95	14.49	0.41	3.36
II	326.93	20.03	6.86	4226.24	4.80	273.21	4.99	0.31	6.68
III	310.81	16.79	6.61	3291.09	5.95	234.84	7.15	0.33	4.81
IV	261.55	16.04	5.85	4998.20	5.33	145.82	18.89	0.46	4.18
<i>Avg.</i>	301.10	17.04	6.42	3585.66	5.02	210.20	11.38	0.38	4.76

to predict different effective moduli across distortion modes, consistent with experimental observations [125]. However, considered individually, these parameters do not carry direct physical meaning.

In Fig. 6(a), corresponding to the 1% w/v gel, both the compressive and tensile responses exhibit low stiffness, and the tensile response exhibits limited strain-stiffening. This behavior is consistent with the sparse polymer network and low cross-link density, which permit extensive chain mobility and low resistance to deformation [114, 167]. The fitted parameters (Table 3) reflect this: a low average μ of 49.79 kPa shows high compliance and low average a of 3.22 kPa indicates limited strain-dependent reinforcement.

Further, the small average tensile pseudo-failure energy ($\Phi^+ = 0.47$ kPa) and large softening sharpness parameter ($m^+ = 139.22$) imply an abrupt loss of load-carrying capacity near failure, characteristic of brittle-like rupture. Because $m^+ \gg 1$, the pseudo-failure energy Φ^+ closely approximates the true failure energy ψ_f^+ in tension (see Eq. (32)), as the stress drop occurs over a narrow energy range. In contrast, for compression, where $m^- \ll 1$, the compressive pseudo-failure energy Φ^- significantly underestimates the total dissipated energy since the actual failure energy ψ_f^- depends jointly on Φ^- and m^- , reflecting a more gradual softening behavior. The associated failure energies (Table 4)— $\psi_f^+ = 0.46$ kPa and $\psi_f^- = 8.76$ kPa—highlight a strong asymmetry, with failure energy nearly 19 times greater in compression than in tension.

At 2% w/v (Fig. 6(b)), both stiffness and nonlinearity increase markedly, consistent with higher cross-link density and reduced chain mobility. The higher average elastic parameters, $\mu = 174.37$ kPa and $a = 6.95$ kPa, suggest enhanced network reinforcement. The increase in average Φ^+ and Φ^- (to 1.78 kPa and 4.03 kPa, respectively) demonstrates increased energy storage and delayed damage initiation. At the same time, the failure energies— $\psi_f^+ = 1.75$ kPa and $\psi_f^- = 25.29$ kPa—show an order-of-magnitude increase from the 1% w/v gel, confirming stronger and more energy-dissipative network connectivity.

At 3% w/v (Fig. 6(c)), the gels exhibit pronounced nonlinearity, high stiffness, and more gradual softening before failure. The stiffer response ($\mu = 301.10$ kPa) and an elevated a value of 17.04 kPa point to reduced molecular mobility and strain-hardening effects within a densely cross-linked network. The pseudo-failure energy parameters increase substantially ($\Phi^+ = 5.02$ kPa, $\Phi^- = 11.38$ kPa), consistent

Table 4: Failure energies for each test sample and the averages within each concentration.

sample	ψ_f^+ (kPa)	ψ_f^- (kPa)
1% w/v		
I	0.52	8.18
II	0.41	9.26
III	0.42	8.28
IV	0.48	9.33
<i>Avg.</i>	0.46	8.76
2% w/v		
I	1.83	25.09
II	1.60	25.18
III	2.29	25.34
IV	1.29	25.54
<i>Avg.</i>	1.75	25.29
3% w/v		
I	3.97	43.79
II	4.79	41.99
III	5.93	44.62
IV	5.31	44.54
<i>Avg.</i>	5.00	43.74

ψ_f^\pm are derived from Φ^\pm and m^\pm (Eq. (32)).

with greater toughness and improved load-bearing capacity. The corresponding failure (i.e., saturation) energies (Table 4)— $\psi_f^+ = 5.00$ kPa and $\psi_f^- = 43.74$ kPa—further highlight the large TCA.

Although the average m^+ at 3% w/v increased (to ~ 210), no systematic trend in m^+ is observed across concentrations, indicating that the sharpness of tensile failure—i.e., the abruptness of post-peak decay—is largely insensitive to bulk gel concentration. In contrast, the average m^- increases consistently from 1% w/v to 3% w/v. This trend does not imply a direct monotonic change in the steepness of compressive softening when comparing concentrations, since m^- acts in concert with the intact stored energy $W(\lambda)$ and the pseudo-failure energy Φ^- , both of which also increase with concentration. Rather, the fitted parameters indicate that stiffer, more densely cross-linked gels sustain higher compressive energies prior to the onset of relatively rapid softening, with m^- modulating how sharply the stress-reduction factor $\text{Red}(\lambda)$ (Eq. (43d)) activates as $W(\lambda)$ approaches Φ^- .

The role of softening sharpness parameters is further clarified in Supplementary Section S.1, which presents a plot to illustrate the influence of m^\pm on the evolution of stress-reduction factors with uniaxial stretch for fixed values of Φ^\pm . From this figure, larger values of m^\pm produce a sharper and more abrupt drop once the stored energy approaches the corresponding pseudo-failure energies (Φ^\pm). This confirms that m^\pm governs the activation and steepness of the softening profile. However, because the actual softening profile also depends on other model parameters, a monotonic reduction or increase in m^\pm across different gel concentrations does not necessarily translate to more gradual or abrupt softening (across these groups).

Across all concentrations, the compressive failure energies exceed their tensile counterparts by nearly an order of magnitude, confirming the strong TCA intrinsic to the agarose network microstructure [9]. The fitted residual errors remain below 10% for all datasets, demonstrating stable and accurate calibration of the proposed asymmetric-failure formulation.

Taken together, these results highlight a central advantage of the proposed asymmetric-failure framework: each model parameter carries clear physical meaning and maps directly onto measurable aspects of macroscopic and microscopic behavior. The elastic parameters μ and a govern the initial stiffness and nonlinear strain-stiffening response, reflecting polymer network connectivity and chain extensibility. b_0

and b_1 govern TCA in elastic response. The failure parameters Φ^\pm and m^\pm link directly to the limiting strain-energy capacity and the abruptness of post-peak softening, providing quantitative access to experimentally derived failure energies (ψ_f^\pm). In this way, the model yields not only accurate macroscopic predictions but also mechanistic insight into microstructural features such as polymer density, cross-link distribution, and mode-dependent failure pathways.

For the agarose hydrogels examined here, these physical interpretations manifest clearly: increasing concentration systematically elevates μ and a , consistent with a stiffer, more tightly connected polymer network with reduced chain extensibility [178, 179, 180]; simultaneously, the growth of Φ^\pm and ψ_f^\pm reflects enhanced toughness and greater energy dissipation prior to rupture [181, 105, 182]. A detailed quantitative assessment of these concentration-dependent trends and parameter interrelations is presented in Section 6.5, using power-law scaling relationships.

6.2. Comparison of softening mechanisms with the classical energy-limiting model

To further highlight the asymmetric softening mechanisms captured by the proposed model, we compare its predicted stress-reduction behavior with that of the classical energy-limiting hyperelastic formulation of Volokh (Section 2.2). For this comparison, we calibrated the Volokh model parameters (paired with the Prasad–Kannan intact strain energy density) using only the tensile data from a representative 3% w/v agarose specimen, following standard practice for single-limiter energy-based models. The predicted tensile and compressive stress–stretch responses, together with the associated stress-reduction factor $\text{Red}(\lambda)$ (Eq. (17)), are shown in Figure 7. The corresponding stress–stretch responses and stress-reduction factors (Eqs. (43b) (tension) and (43d) (compression)) from the proposed asymmetric formulation are also shown for comparison. In both formulations, the reduction factor governs the decay of the intact hyperelastic response during damage accumulation.

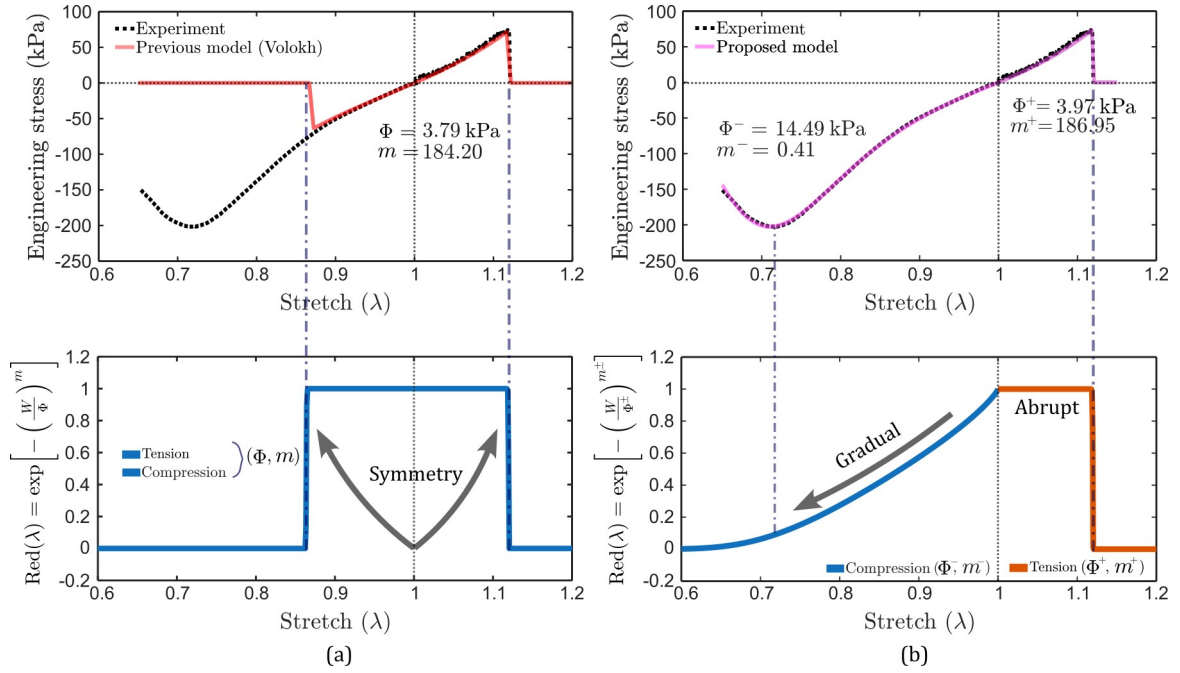


Figure 7: Comparison of experimental (black) and model-predicted (red and magenta) engineering stress–stretch responses for a 3% agarose specimen. (a) The classical Volokh model (red) employs a single set of failure parameters (Φ, m), yielding symmetric softening in tension and compression. (b) The proposed asymmetric-failure formulation (magenta) introduces mode-specific pseudo-failure energies (Φ^+, Φ^-) and corresponding softening sharpness parameters (m^+, m^-). The resulting reduction factors exhibit abrupt decay in tension and gradual decay in compression, consistent with the observed TCA.

In the intact elastic regime, the stored energy W remains small relative to the pseudo-failure energies (i.e., Φ in the Volokh model, and Φ^\pm in the proposed model). Consequently, both formulations yield stress-reduction factors close to unity (i.e., $\exp\left[-\left(\frac{W(\lambda)}{\Phi}\right)^m\right] \approx \exp\left[-\left(\frac{W(\lambda)}{\Phi^\pm}\right)^{m^\pm}\right] \approx 1$, indicating negligible softening. Beyond this small-strain regime, however, the two models diverge sharply in their predictions of tensile and compressive softening.

Because the Volokh model employs a single pseudo-failure energy Φ and a single softening sharpness parameter m for all loading modes, it predicts identical decay of $\text{Red}(\lambda)$ in tension and compression. As

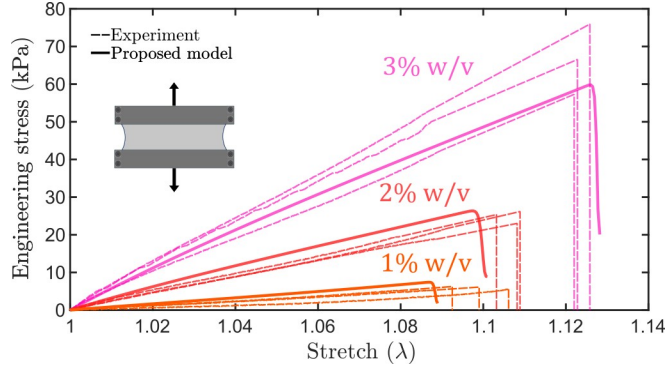


Figure 8: Engineering stress–stretch response for agarose gel specimens in pure shear. Dashed lines represent experimental data ($n = 3$) for 1%, 2%, and 3% w/v specimens. Solid lines show the corresponding predictions of the proposed model using parameters calibrated solely from combined uniaxial compression–tension data.

shown in Fig. 7(a), tensile and compressive responses exhibit a symmetric softening trajectory, and the predicted compressive response fails to reproduce the experimentally observed gradual loss of stiffness. Furthermore, the Volokh model underestimates the higher failure energy in compression, a hallmark of TCA in soft materials. These deficiencies arise from the inherent symmetry imposed by a single set of energy limiters.

In contrast, the proposed model introduces mode-specific pseudo–failure energies Φ^\pm and softening sharpness parameters m^\pm , enabling distinct decay patterns of $\text{Red}(\lambda)$. In tension, a large $m^+ \gg 1$ keeps $\text{Red}(\lambda) \approx 1$ over most of the deformation path until $W \approx \Phi^+$, after which it drops abruptly, reproducing the sharp tensile rupture observed experimentally. In contrast, in compression, with $m^- < 1$, even modest increases in W cause a smooth, gradual decay of $\text{Red}(\lambda)$, matching the progressive softening and high failure energy seen in experiments. Figure 7(b) highlights this sharp contrast—an abrupt decay under tension and a gradual reduction under compression—demonstrating that the asymmetric formulation naturally encodes the experimentally observed TCA in softening and failure behavior.

6.3. Generalizability of the proposed model: performance in pure shear

To evaluate the model’s generalizability beyond uniaxial loading, we next examined its predictive capability under pure shear—a deformation mode with fundamentally different distortional kinematics and stress state. For this analysis, the average calibrated parameters for each concentration (1, 2, and 3% w/v) obtained strictly from the combined tension–compression datasets (Table 3) were used directly to predict the pure shear response (using Eq. (49)), without any additional fitting.

As shown in Figure 8, the predicted stress–stretch curves exhibit excellent agreement with experimental data across all concentrations (1%, 2%, and 3% w/v). The initial shear stiffness, the onset and progression of softening, and the failure stretch and stress values closely match the measured trends. The transition from intact elasticity to damage is governed by the same asymmetric pseudo–failure energies Φ^\pm and sharpness parameters m^\pm identified from uniaxial tests, while the Lode-invariant weighting function $\beta(K_3)$ naturally adjusts their influence under pure shear. This produces a seamless extension of the uniaxially calibrated constitutive behavior into a distinct distortional mode.

Minor deviations in the post-peak response likely stem from localized instabilities or geometric effects not explicitly accounted for in the present homogeneous continuum formulation. Nonetheless, the model successfully captures the concentration-dependent increase in shear stiffness and failure stress, consistent with the higher cross-link density at elevated agarose concentrations.

Overall, this validation demonstrates that the proposed Lode-invariant-based asymmetric energy-limiting model, calibrated solely from uniaxial data, can accurately predict the mechanical response of agarose hydrogels under an entirely different distortional mode. The ability to reproduce both elastic and inelastic features across deformation paths without additional fitting highlights the robustness and generalizability of our proposed framework.

6.4. Free-energy landscape of the proposed model

Having established the predictive capability of the proposed model under pure shear, we now examine its free-energy landscape to reveal how TCA emerges within the invariant space. Visualizing the evolution of the proposed potential ψ_{prop} (Eq. (36)) over the distortional invariants K_2 (magnitude) and K_3 (mode) provides direct mechanistic insight into how failure energy varies across distortion modes in a smooth

and thermodynamically consistent manner—thereby linking the responses of uniaxial tension, pure shear, and uniaxial compression within a unified representation.

The proposed strain energy density ψ_{prop} was evaluated by first computing the intact stored energy density $W(K_2, K_3)$ from the Prasad–Kannan hyperelastic framework [125], followed by mapping this energy through the proposed energy-limiting function (Eq. (36)). This mapping, governed by the mode-dependent energy limiters Φ^\pm and m^\pm and the Lode-angle-based weighting function $\beta(K_3) \in [0, 1]$, ensures a continuous interpolation between the tensile and compressive failure energies. Consequently, ψ_{prop} varies intrinsically with the deformation mode, capturing the physical dependence of failure energy on the distortional state rather than enforcing a uniform limit across all modes.

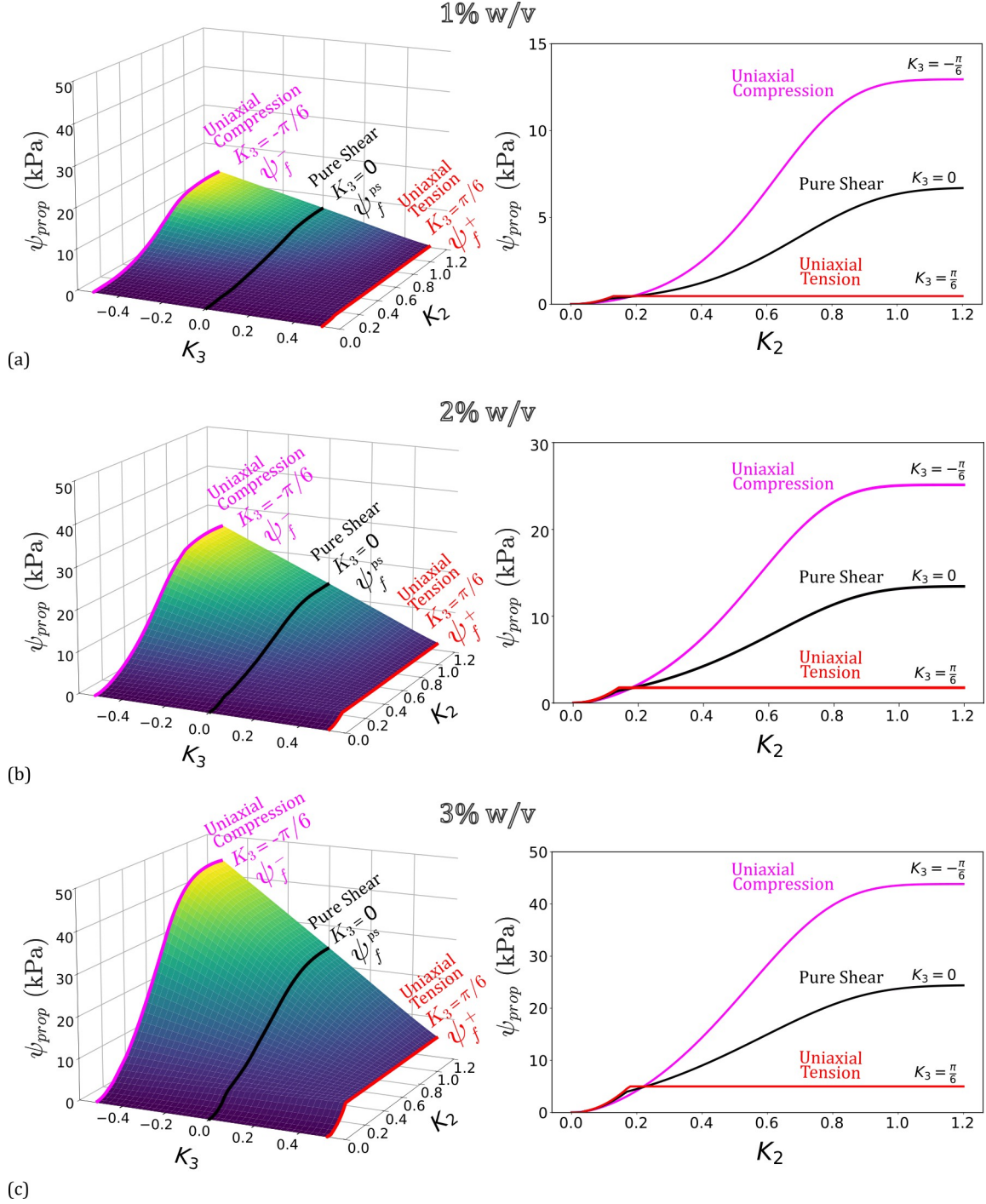


Figure 9: Free-energy landscapes of ψ_{prop} for agarose gels at (a) 1% w/v, (b) 2% w/v, and (c) 3% w/v. Left column: $\psi_{\text{prop}}(K_2, K_3)$ surfaces over the $K_2 - K_3$ invariant space. Right column: corresponding $\psi_{\text{prop}}(K_2)$ slices at $K_3 = \{-\pi/6, 0, \pi/6\}$, representing uniaxial compression (magenta), pure shear (black), and uniaxial tension (red).

Figure 9 presents the resulting energy landscapes for agarose gels at 1%, 2%, and 3% w/v concentrations. The left panels illustrate the three-dimensional variation of ψ_{prop} over the (K_2, K_3) invariant domain, while the right panels show characteristic two-dimensional $\psi_{\text{prop}} - K_2$ slices at $K_3 = \{-\pi/6, 0, \pi/6\}$, corresponding respectively to uniaxial compression, pure shear, and uniaxial tension. The computational domain spans the physically admissible range of Lode invariants: K_2 varies from zero (undeformed) to a large distortional magnitude (i.e., $K_2 = 1.2$), and K_3 spans from compression- to tension-dominant states.

Across all concentrations, the surfaces reveal a clear and systematic TCA across concentrations: the saturation energy is consistently highest in compression ($K_3 = -\pi/6$) and lowest in tension ($K_3 = +\pi/6$), mirroring the experimental observation that agarose sustains and dissipates substantially greater energy before failure in compression. Intermediate deformation modes transition smoothly between these bounds, confirming that the Lode-invariant-based interpolation introduces no discontinuities or artificial artifacts.

Importantly, no regions of singularity or discontinuous curvature are observed across the energy surfaces, even near the failure envelopes. This continuity indicates that the constitutive formulation maintains bounded energy derivatives ($\partial\psi/\partial K_2, \partial\psi/\partial K_3$), ensuring mechanical stability and preventing nonphysical responses such as snap-back or abrupt stiffness loss [183, 184, 185, 186]. The continuous and convex topology of the energy landscape thus validates the internal consistency of the model and confirms that the Lode-invariant interpolation remains thermodynamically admissible across all deformation paths [187, 148, 188].

For any fixed deformation mode K_3 , the potential increases monotonically with K_2 , demonstrating that K_2 governs the magnitude of stored energy accumulation, while K_3 modulates the attainable energy limit and the manner of failure (e.g., gradual versus abrupt). The pure shear response ($K_3 = 0$) naturally interpolates between the tensile and compressive bounds, yielding an intermediate softening trajectory consistent with the experimental observations presented earlier.

As concentration increases from 1% to 3% w/v, both the magnitude and curvature of ψ_{prop} increase, reflecting the stiffness and enhanced failure thresholds of denser agarose networks [180]. The enhanced energy storage capacity and greater asymmetry at higher concentrations are consistent with the densification and strengthening of the polymer network [179, 105, 9], as previously observed in the stress-stretch data (Figs. 6 and 8).

Overall, the free-energy landscapes show that the proposed Lode-invariant-based formulation produces a physically interpretable, mode-sensitive, and thermodynamically stable potential. By unifying the tensile, compressive, and intermediate mixed-mode energy responses within a single framework, the model provides a mechanistic foundation for the asymmetric softening and failure behaviors quantified in the preceding sections.

6.5. Power-law parameter scaling and predictive cross-concentration validation at 2.5% w/v

Having established the model’s accuracy and stability across deformation modes, we now assess its scalability across agarose gel concentrations. This subsection aims to (i) quantify how each calibrated model parameter evolves with gel concentration using power-law scaling, and (ii) use these scaling relationships to predict the constitutive response of an intermediate concentration (2.5% w/v) that was not used during calibration. Successful prediction of uniaxial and pure shear responses at this interpolated composition provides a stringent test of cross-concentration generalizability.

The concentration-dependent evolution of each model parameter (Y) was fitted using a power-law relationship of the form:

$$Y = K c^n, \quad (52)$$

where c denotes gel concentration, K is a scaling constant, and n represents the power-law exponent. The data were linearized using logarithmic transformation,

$$\log(Y) = \log(K) + n \log(c), \quad (53)$$

and fitted in MATLAB using a linear model (`poly1`). Here, n is the slope of the log-log plot, and $\log(K)$ is the intercept, which yields the scaling factor via $K = \exp(\log(K))$.

Figure 10 shows the resulting power-law fits for the eight model parameters— $\mu, a, b_0, b_1, \Phi^\pm$, and m^\pm —for 1%, 2%, and 3% w/v agarose gels (parameters are listed in Table 3). Error bars represent one standard deviation. The instantaneous shear modulus μ exhibits a strong positive scaling ($\mu \sim c^{1.66}$), consistent with the expected stiffening behavior of polymer networks with concentration [114, 132, 105, 189, 190]. Similarly, the strain-stiffening parameter $a \sim c^{1.47}$ indicates increasing nonlinear reinforcement

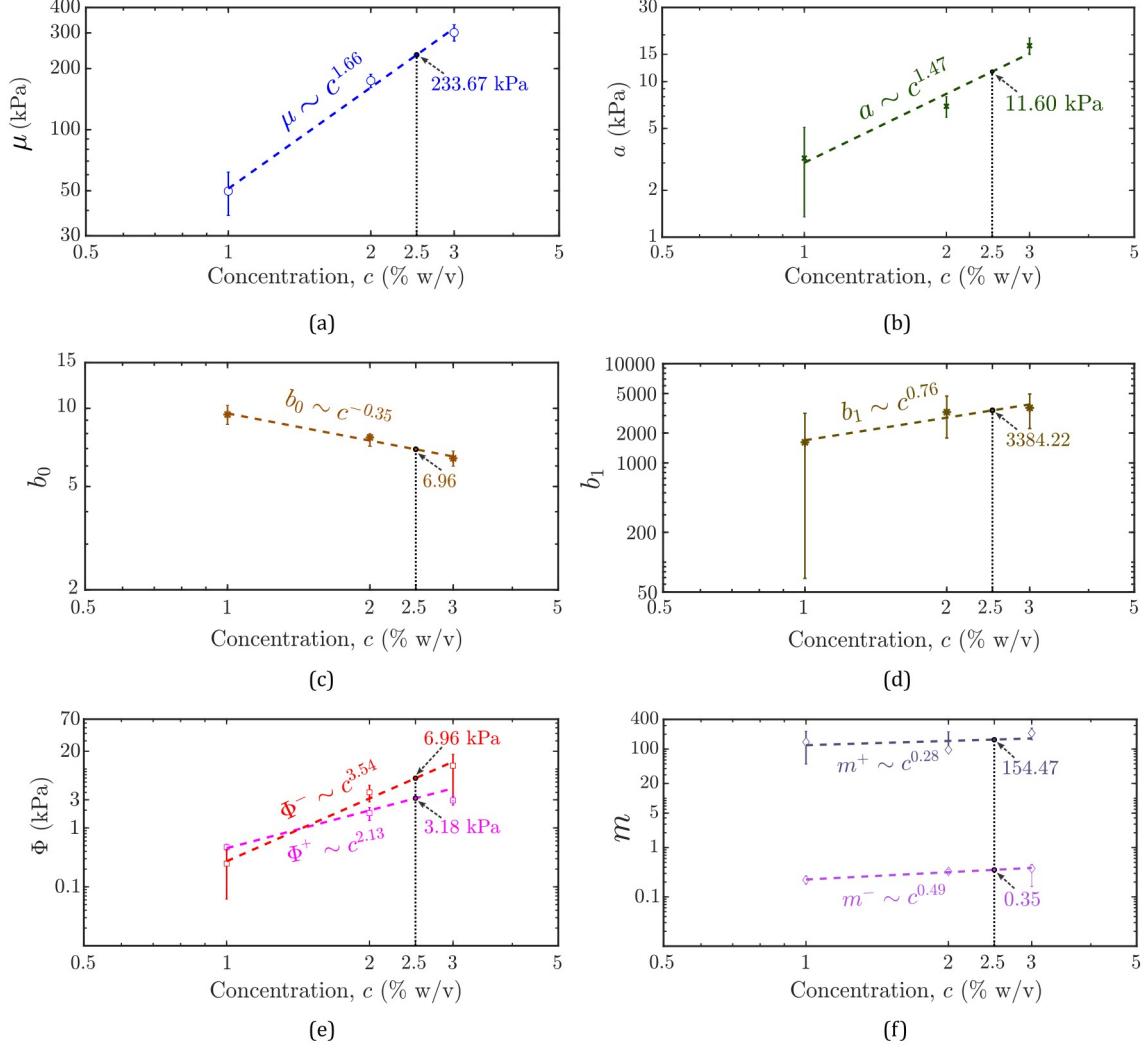


Figure 10: Evolution of the proposed model’s parameters with agarose gel concentration (from Table 3). (a) Infinitesimal shear modulus μ ; (b) nonlinear strain-stiffening parameter a ; (c) b_0 and (d) b_1 , parameters defining the mode-dependent modulus function $\mathcal{G}(K_3)$; (e) tensile and compressive pseudo-failure energy parameters Φ^+ and Φ^- ; and (f) tensile and compressive softening sharpness parameters m^+ and m^- . Remember, all parameters were obtained from simultaneous tension-compression fitting. Error bars represent one standard deviation. Dotted lines show power-law fits; power law exponents and interpolated values at 2.5% w/v are highlighted.

with concentration, reflecting a progressive amplification of strain-dependent shear response [9]. The modulus-function constants b_0 and b_1 exhibit weaker trends ($b_0 \sim c^{-0.35}$, $b_1 \sim c^{0.76}$), implying that the shape of the mode-dependent stiffness modulation varies only modestly across concentrations.

The tensile and compressive pseudo-failure energy parameters $\Phi^+ \sim c^{2.13}$ and $\Phi^- \sim c^{3.54}$ grow substantially with concentration, reflecting increased failure energies and enhanced load-transfer capacity in denser networks. Further, they exhibit distinct scaling trends, with Φ^- showing a steeper scaling with concentration, echoing the stronger energy-dissipation capacity in compression, with microstructural densification and enhanced load transfer through the polymer network at higher concentrations (see Section 3). The tensile softening sharpness parameter m^+ shows no systematic trend while the compressive softening sharpness parameter m^- shows a weak positive scaling, consistent with earlier observations.

The interpolated parameter values at 2.5% w/v, listed in Table 5 and highlighted in the figure,

Table 5: Estimated model parameters of 2.5% w/v agarose from power-law relationship.

μ (kPa)	a (kPa)	b_0	b_1	Φ^+ (kPa)	m^+	Φ^- (kPa)	m^-
233.67	11.60	6.96	3384.22	3.18	154.47	6.96	0.35

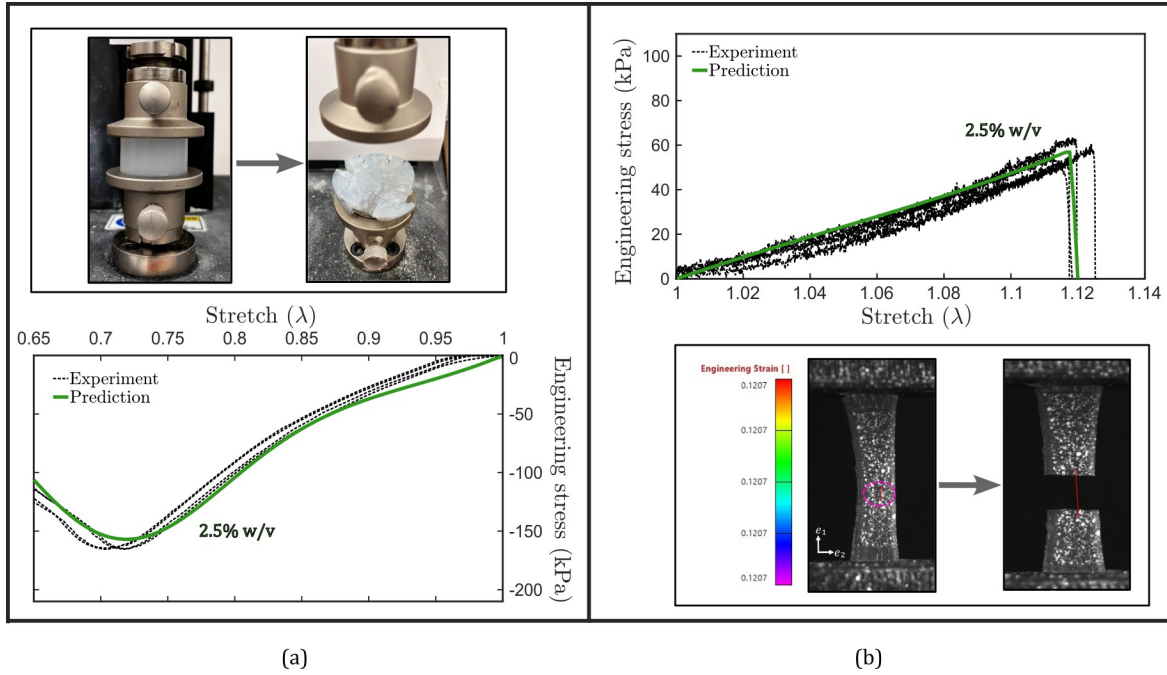


Figure 11: Experimental ($n=4$) and predicted engineering stress versus stretch plots of 2.5% w/v agarose hydrogel in a) compression and b) tension. Predictions use parameters obtained solely from power-law interpolation of 1–3% w/v data. Tensile strain was measured using DIC-based virtual extensometer.

provide an intermediate reference dataset for predictive validation. Using these interpolated values, we predicted the mechanical response of 2.5% w/v gels under both uniaxial and pure shear loading without any additional fitting. As shown in Fig. 11, the predicted tensile and compressive responses agree closely with experiments, accurately capturing the elastic response, softening behavior, and failure onset. This agreement confirms that the power-law scaling effectively bridges concentration-dependent material behavior within the proposed asymmetric energy limiters framework.

Figure 12 extends this validation to the pure shear, a deformation path that was not used in the original parameter calibration. The ability of the interpolated parameters to accurately reproduce the elastic, softening, and failure responses under this unseen distortional mode demonstrates the robustness of the concentration-scaling framework. Together with the uniaxial results, the close agreement in pure shear confirms the framework’s *cross-concentration* and *cross-deformation-mode* generalizability.

Overall, the power-law scaling analysis provides a physically grounded and compact description of how elastic and failure parameters evolve with concentration. Combined with the validated cross-mode predictions, these results underscore the model’s capability to unify stiffness evolution, softening behavior, and failure energetics across both compositional and kinematic spaces, setting the stage for future application to other soft polymeric materials.

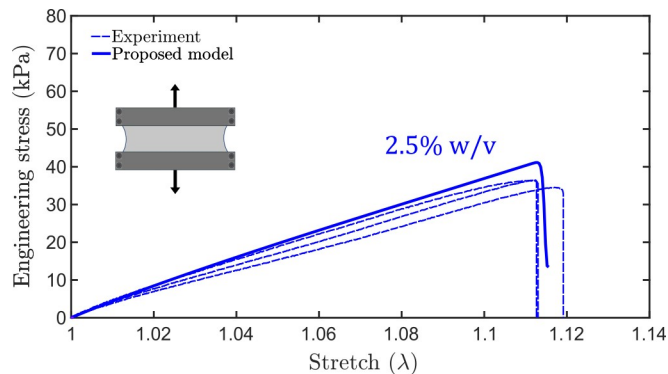


Figure 12: Engineering stress–stretch response of 2.5% w/v agarose hydrogel in pure shear. Dashed lines represent experimental data ($n=3$), while the solid line represents prediction from the proposed model using power-law-interpolated parameters.

7. Summary and Conclusion

Soft materials such as elastomers, hydrogels, and biological tissues exhibit pronounced TCA in their damage and failure responses—an aspect inadequately captured by most existing hyperelastic softening formulations. Motivated by this limitation, the present work introduces a generalized constitutive framework that extends Volokh’s energy-limiting theory to explicitly incorporate TCA through a physically motivated, distortion–mode–dependent softening formulation. The proposed model exploits the physical interpretability of the invariants of the logarithmic (Hencky) strain tensor—particularly the Lode invariants (K_2, K_3) [125, 127, 122, 121]—to decompose the failure energy into distinct tensile and compressive branches. This bifurcation establishes an analytically driven switching criterion that allows independent control of distortion–mode–sensitive softening, thereby improving model generality and predictive capability across different loading modes while maintaining thermodynamic consistency. Notably, the use of alternative, non-orthogonal invariant measures would preclude such a bi-failure construction, as deriving a mathematically consistent expression for mode-dependent energy saturation becomes intractable without the Lode-invariant framework.

To represent the intact (undamaged) response, the proposed asymmetric-failure formulation incorporates the Prasad–Kannan hyperelastic potential [125], originally developed from brain tissue experimental data and derived through an *a priori* enforcement of the B–E inequalities [150]. Within this framework, the complete constitutive description comprises eight parameters—four governing the elastic response and four regulating failure energetics. The model was calibrated using combined uniaxial tension and compression data for agarose gels at concentrations from 1–3% w/v. Unlike conventional single-mode calibrations, the simultaneous fitting across both deformation modes is enabled by the Lode-invariant energy limiters, enabling a unified and physically motivated, distortion-mode-aware representation of both the intact hyperelastic response and its associated softening behavior.

The framework demonstrated two levels of predictive capability. First, a multi-deformation-mode generalizability was established, wherein the model accurately predicted the pure shear response at each concentration (1, 2, and 3 % w/v) using parameters calibrated solely from combined uniaxial tension–compression data. Second, an independent predictive validation was performed at 2.5 % w/v by computing model parameters through power-law interpolation of fitted parameters from the 1–3 % w/v range. The predicted stress–stretch responses for all three primary distortion modes showed excellent agreement with experiments, confirming both cross-concentration and cross-mode predictive accuracy of the proposed theory.

A key feature of the framework is the introduction of mode-dependent energy limiters (i.e., pseudo-failure energies (Φ^\pm) and softening sharpness parameters (m^\pm)) governing both elastic storage and dissipation. This establishes a direct and physically interpretable link between microstructural failure mechanisms and macroscopic continuum-level behavior—without invoking any internal state variables. The calibrated parameters reliably represent essential microstructural mechanisms associated with rupture and energy dissipation, yielding a continuous and mechanistically grounded representation of softening. Such interpretability, long recognized as central to constitutive modeling [191, 192, 193], enhances both predictive fidelity and transparency while offering insight into how network architecture influences progressive damage. The agarose gels studied here serve as bio-mimetic surrogates, establishing a foundation for probing tissue-like failure mechanisms in a controlled environment [194, 195, 196].

Looking ahead, the proposed framework can be extended to construct a comprehensive three-dimensional failure map over the (K_2, K_3) invariant space. This advancement would require systematic multi-axial testing—such as combined compression–shear loading or energetically exhaustive protocols like unequal biaxial deformation [128]—to capture a complete representation of the energy surface and unveil the entire failure envelope of the material. Such experiments would enable direct evaluation of the Lode-weighting function $\beta(K_3)$, which in the present study was assumed to vary linearly based on validation across the three primary distortional modes. Incorporating these experimental insights would refine this assumption and facilitate a more accurate, data-driven characterization of mode-dependent failure energetics, thereby advancing toward a unified and comprehensive description of soft-material damage across the entire distortional domain.

Declaration of competing Interest

The authors declare that they have no known competing financial interests or personal relationships that could have appeared to influence the work reported in this paper.

Acknowledgements

This material is based upon work supported by the National Science Foundation under Grant No. 2331294.

Data availability

Data will be made available on request.

Appendix A. Tensor basis components of the Cauchy stress in Lode-invariants-based hyperelasticity

Mutually orthogonal unit kinematic tensors derived from Lode invariants and the left stretch tensor \mathbf{V} for an incompressible material [125, 12]:

$$\mathbf{N}_1 = \frac{\partial K_2}{\partial \ln \mathbf{V}} = \frac{\text{dev}(\ln \mathbf{V})}{K_2}, \quad (\text{A.1})$$

$$\mathbf{N}_2 = K_2 \frac{\partial K_3}{\partial \ln \mathbf{V}} = \frac{\sqrt{6}}{\cos(3K_3)} \left(\mathbf{N}_1^2 - \frac{1}{3} \mathbf{I} - \text{tr}(\mathbf{N}_1^3) \mathbf{N}_1 \right) \quad (\text{A.2})$$

Appendix B. On irreversibility in hyperelasticity with energy limiters

The energy-limiting formulation proposed by Volokh [41, 43, 120] in Eq. (11) provides a framework for incorporating material failure into hyperelastic models. However, in its standard reversible form, the softening response remains path-independent: upon unloading, the material can elastically recover to its original state. This reversibility limits its physical realism, as actual material failure is inherently irreversible once the energy threshold is exceeded.

To impose irreversibility and path dependency, Volokh [166] introduced a switch parameter ζ through a Heaviside step function that permanently restricts the recoverable energy once the failure energy density ψ_f is reached. The modified stored-energy function is expressed as:

$$\psi(W(\mathbf{F}), \zeta) = \psi_f - H(\zeta) \psi_e(W(\mathbf{F})), \quad (\text{B.1})$$

where ψ_e denotes the elastic strain energy and $H(\zeta)$ is the Heaviside function governing the transition between reversible and irreversible states.

The evolution of the switch parameter $\zeta \in (-\infty, 0]$ is defined by

$$\dot{\zeta} = -H\left(\epsilon - \frac{\psi_e}{\psi_f}\right), \quad \zeta(0) = 0, \quad (\text{B.2})$$

where ϵ is a small dimensionless tolerance parameter ($0 < \epsilon \ll 1$) introduced to avoid numerical singularities near the energy limit.

In this formulation, the Heaviside function $H(\zeta)$ acts as a state-locking mechanism:

$$H(\zeta) = \begin{cases} 1, & \text{for } \zeta \geq 0 \quad (\text{reversible region}), \\ 0, & \text{for } \zeta < 0 \quad (\text{irreversible region}). \end{cases}$$

When $\psi_e < \psi_f$, the system remains in the reversible regime ($\zeta = 0$, $H(\zeta) = 1$), and deformation is purely hyperelastic. Once ψ_e attains the failure threshold ψ_f , the variable ζ becomes negative, enforcing $H(\zeta) = 0$. The strain energy is then locked at ψ_f , thereby preventing further recovery upon unloading and ensuring irreversible energy dissipation [166, 197, 101].

Thus, ζ does not evolve continuously like an internal damage variable; rather, it acts as a discrete state switch that governs the transition from reversible to irreversible deformation. This treatment introduces path dependence into the otherwise elastic framework, ensuring that once failure occurs, the material cannot regain its original stored-energy capacity.

Appendix C. Pure Shear stress–stretch reconstruction up to failure

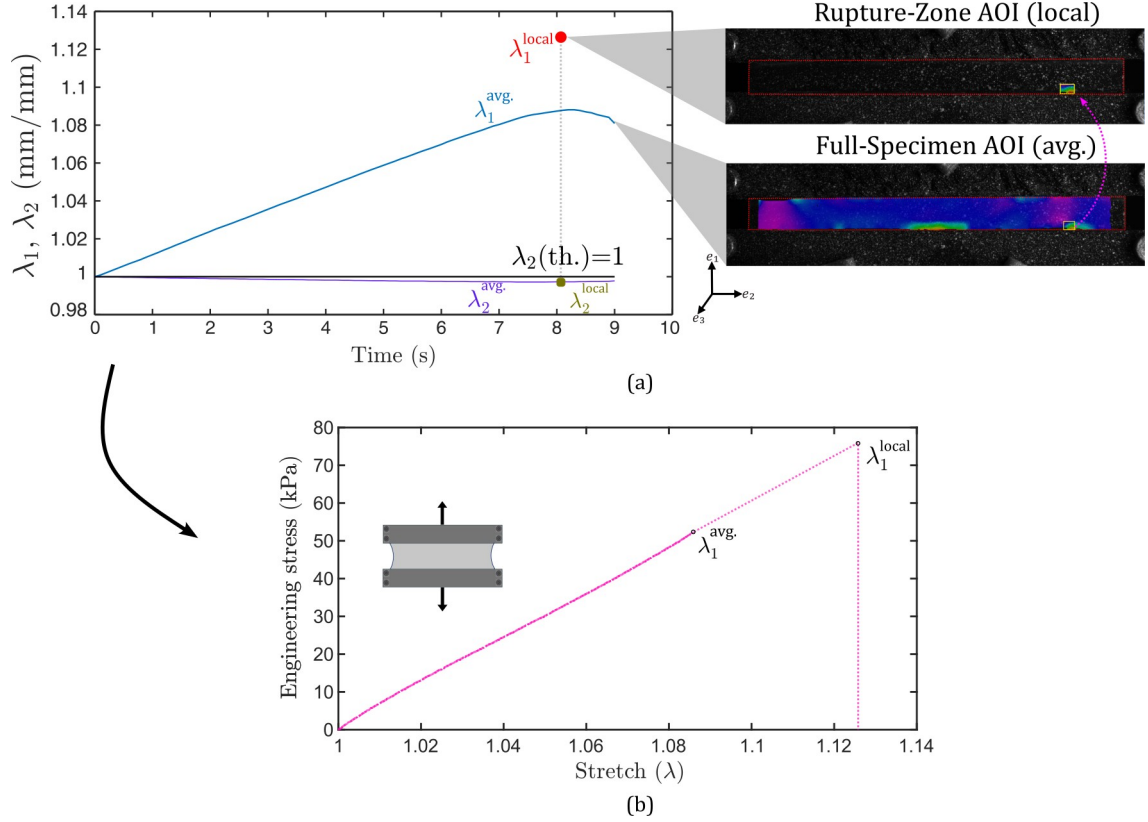


Figure C.13: (a) In-plane principal stretches λ_1 (axial) and λ_2 (transverse) extracted from the average full-specimen AOI (avg.) and from a small local AOI positioned at the eventual rupture site (local). Both AOIs satisfy the pure shear condition $\lambda_2 \approx 1$, consistent with the mapping introduced in Section 2.1. The local AOI provides the avg. stretch immediately prior to rupture. (b) Engineering stress–stretch response reconstructed by pairing the avg. engineering stress with the avg. stretch during the homogeneous regime and extrapolated to the local rupture stretch λ_1^{local} at the failure instant.

Figure C.13 summarizes the procedure to obtain a consistent pure shear stress–stretch response up to rupture. The method relies on two key observations:

1. **Pure shear kinematics in both AOIs.** The evolution of the in-plane strain components ($\varepsilon_{11} = \lambda_1 - 1$, $\varepsilon_{22} = \lambda_2 - 1$) extracted from the average strain contour of the full-specimen AOI shows that the transverse stretch remains close to unity ($\lambda_2^{\text{avg}} \approx 1$) throughout the loading history, confirming that the specimen maintains an ideal pure shear state during the homogeneous deformation phase. Immediately before rupture, the locally measured stretches at the failure site (λ_1^{local} , λ_2^{local}) also satisfy $\lambda_2^{\text{local}} \approx 1$, indicating that the deformation field at the rupture location remains consistent with the incompressible pure shear mapping $\{\lambda, 1, \lambda^{-1}\}$ introduced in Section 2.1 (Eqs. (8)–(9)). Accordingly, both AOIs provide kinematically admissible descriptions of the deformation state: the avg. AOI captures the global homogeneous response, whereas the local AOI furnishes the appropriate stretch measure at the point of failure.
2. **Localization and local stretch at failure.** As rupture approaches, strain localizes in a small region of the specimen, causing the local axial stretch to deviate from the global, spatially averaged response. The avg. AOI continues to characterize the homogeneous deformation portion of the test, while the local AOI isolates the stretch at the failure site. The rupture stretch λ_1^{local} is therefore taken directly from the local AOI at the final pre-rupture frame and appended to the avg. stretch history to complete the deformation trajectory.

Importance of Using Average Engineering Stress–Stretch Before Localization

The engineering stress during pure shear is obtained from the measured load-cell force divided by the cross-sectional area (height H between the clamps and specimen width W ; see Fig. 2). Because this load corresponds to the *global* planar tensile force acting on the entire section, the associated strain

measure must likewise represent a global deformation. Pairing a global stress with a local strain value would be inconsistent and would artificially distort the stress–stretch response, especially in materials such as hydrogels where deformation fields may be spatially non-uniform due to material heterogeneity or slight loading inhomogeneities [198, 199].

2D-DIC provides a full-field measure of the deformation and enables the computation of spatially averaged principal stretches across the entire gauge region. As reported in prior analyses of shear tests by Millar et al. [198], averaging the strain field over the full-specimen AOI yields the most reliable representation of the global shear response, particularly when shear and normal strain distributions vary across the width.

Once the avg. engineering stretch λ_1^{avg} has been paired consistently with the corresponding global engineering stress during the homogeneous regime, the final local rupture stretch λ_1^{local} is appended to the avg. curve to extend the stress–stretch response to the rupture point. This procedure ensures that:

- the stress is always paired with a physically meaningful strain measure,
- global deformation is represented accurately up to the onset of localization, and
- the final point on the curve reflects the true local strain at the site of material failure.

The resulting complete stress–stretch response, shown in Fig. C.13(b), is therefore consistent with pure shear kinematics throughout loading and remains suitable for validation of the proposed constitutive model up to failure.

References

- [1] A. Goriely, M. G. Geers, G. A. Holzapfel, J. Jayamohan, A. Jérusalem, S. Sivaloganathan, W. Squier, J. A. van Dommelen, S. Waters, E. Kuhl, Mechanics of the brain: perspectives, challenges, and opportunities, *Biomechanics and modeling in mechanobiology* 14 (5) (2015) 931–965.
- [2] D. Böhringer, J. Hinrichsen, R. Gataulin, S. Wiedenmann, M. Spörrer, S. Sherifova, P. Steinmann, G. A. Holzapfel, B. Fabry, S. Budday, Compression-tension-asymmetry and stiffness nonlinearity of collagen-matrigel composite hydrogels, *Advanced Healthcare Materials* (2025) e03052.
- [3] A. Anssari-Benam, M. Destrade, G. Saccomandi, Modelling brain tissue elasticity with the ogden model and an alternative family of constitutive models, *Philosophical Transactions of the Royal Society A* 380 (2234) (2022) 20210325.
- [4] D. Martonová, A. Goriely, E. Kuhl, Generalized invariants meet constitutive neural networks: A novel framework for hyperelastic materials, *Journal of the Mechanics and Physics of Solids* (2025) 106352.
- [5] J.-M. Y. Carrillo, F. C. MacKintosh, A. V. Dobrynin, Nonlinear elasticity: from single chain to networks and gels, *Macromolecules* 46 (9) (2013) 3679–3692.
- [6] G. A. Holzapfel, J. D. Humphrey, R. W. Ogden, Biomechanics of soft biological tissues and organs, mechanobiology, homeostasis and modelling, *Journal of the Royal Society Interface* 22 (222) (2025) 20240361.
- [7] K. M. Moerman, C. K. Simms, T. Nagel, Control of tension-compression asymmetry in ogden hyperelasticity with application to soft tissue modelling, *Journal of the Mechanical Behavior of Biomedical Materials* 56 (2016) 218–228. doi:10.1016/j.jmbbm.2015.11.027.
- [8] K. M. Myers, C. P. Hendon, Y. Gan, W. Yao, K. Yoshida, M. Fernandez, J. Vink, R. J. Wapner, A continuous fiber distribution material model for human cervical tissue, *Journal of biomechanics* 48 (9) (2015) 1533–1540.
- [9] A. D. Drozdov, J. d. Christiansen, Tension–compression asymmetry in the mechanical response of hydrogels, *Journal of the Mechanical Behavior of Biomedical Materials* 110 (2020) 103851.
- [10] D. H. Cortes, D. M. Elliott, Extra-fibrillar matrix mechanics of annulus fibrosus in tension and compression, *Biomechanics and modeling in mechanobiology* 11 (6) (2012) 781–790.

- [11] J.-y. Sun, H.-q. Zhu, S.-h. Qin, D.-l. Yang, X.-t. He, A review on the research of mechanical problems with different moduli in tension and compression, *Journal of mechanical science and technology* 24 (9) (2010) 1845–1854.
- [12] M. Reddipaga, K. Kannan, On the construction of a viscoelastic constitutive model for brain tissue maximizing tension–compression asymmetry, *International Journal of Engineering Science* 218 (2026) 104415.
- [13] X. Huang, B. Li, W. Hong, Y.-P. Cao, X.-Q. Feng, Effects of tension–compression asymmetry on the surface wrinkling of film–substrate systems, *Journal of the Mechanics and Physics of Solids* 94 (2016) 88–104.
- [14] Z. Du, X. Guo, Variational principles and the related bounding theorems for bi-modulus materials, *Journal of the Mechanics and Physics of Solids* 73 (2014) 183–211.
- [15] Z. Du, G. Zhang, T. Guo, S. Tang, X. Guo, Tension-compression asymmetry at finite strains: A theoretical model and exact solutions, *Journal of the Mechanics and Physics of Solids* 143 (2020) 104084.
- [16] S. Tang, G. Zhang, T. F. Guo, X. Guo, W. K. Liu, Phase field modeling of fracture in nonlinearly elastic solids via energy decomposition, *Computer Methods in Applied Mechanics and Engineering* 347 (2019) 477–494.
- [17] P. S. Stewart, S. L. Waters, T. El Sayed, D. Vella, A. Goriely, Wrinkling, creasing, and folding in fiber-reinforced soft tissues, *Extreme Mechanics Letters* 8 (2016) 22–29.
- [18] A. Konale, V. Srivastava, On modeling fracture of soft polymers, *Mechanics of Materials* 206 (2025) 105346.
- [19] K. Volokh, Fracture as a material sink, *Materials Theory* 1 (1) (2017) 3.
- [20] J. Notbohm, A. Lesman, P. Rosakis, D. A. Tirrell, G. Ravichandran, Microbuckling of fibrin provides a mechanism for cell mechanosensing, *Journal of The Royal Society Interface* 12 (108) (2015) 20150320.
- [21] K. Linka, M. Hillgärtner, M. Itskov, Fatigue of soft fibrous tissues: multi-scale mechanics and constitutive modeling, *Acta biomaterialia* 71 (2018) 398–410.
- [22] A. Anssari-Benam, M. Hossain, A unified pseudo-elastic model of continuous and discontinuous softening in the finite deformation of isotropic soft solids, *International Journal of Solids and Structures* 290 (2024) 112670.
- [23] J. A. Peña, M. A. Martínez, E. Peña, Failure damage mechanical properties of thoracic and abdominal porcine aorta layers and related constitutive modeling: phenomenological and microstructural approach, *Biomechanics and Modeling in Mechanobiology* 18 (6) (2019) 1709–1730.
- [24] W. Liu, Z. Yu, K. I. Elkhodary, H. Xiao, S. Tang, T. Guo, X. Guo, A tube-based constitutive model of brain tissue with inner pressure, *Journal of the Mechanics and Physics of Solids* 196 (2025) 105993.
- [25] M. Rausch, G. Karniadakis, J. Humphrey, Modeling soft tissue damage and failure using a combined particle/continuum approach, *Biomechanics and modeling in mechanobiology* 16 (1) (2017) 249–261.
- [26] Z. Zhu, C. Jiang, H. Jiang, A visco-hyperelastic model of brain tissue incorporating both tension/compression asymmetry and volume compressibility, *Acta Mechanica* 230 (6) (2019) 2125–2135.
- [27] K. Upadhyay, A. Alshareef, A. K. Knutsen, C. L. Johnson, A. Carass, P. V. Bayly, D. L. Pham, J. L. Prince, K. T. Ramesh, Development and validation of subject-specific 3D human head models based on a nonlinear visco-hyperelastic constitutive framework, *Journal of The Royal Society Interface* 19 (195) (2022) 1–27. doi:10.1098/rsif.2022.0561.

- [28] P. V. Bayly, A. Alshareef, A. K. Knutsen, K. Upadhyay, R. J. Okamoto, A. Carass, J. A. Butman, D. L. Pham, J. L. Prince, K. T. Ramesh, C. L. Johnson, MR Imaging of Human Brain Mechanics In Vivo: New Measurements to Facilitate the Development of Computational Models of Brain Injury, *Annals of Biomedical Engineering* 49 (10) (2021) 2677–2692. doi:10.1007/s10439-021-02820-0.
- [29] G. Franceschini, D. Bigoni, P. Regitnig, G. A. Holzapfel, Brain tissue deforms similarly to filled elastomers and follows consolidation theory, *Journal of the Mechanics and Physics of Solids* 54 (12) (2006) 2592–2620.
- [30] K. Mendis, R. Stalnakar, S. Advani, A constitutive relationship for large deformation finite element modeling of brain tissue, *Journal of Biomechanical Engineering* (1995).
- [31] M. J. Lohr, G. P. Sugerma, S. Kakaletsis, E. Lejeune, M. K. Rausch, An introduction to the ogden model in biomechanics: Benefits, implementation tools and limitations, *Philosophical Transactions of the Royal Society A: Mathematical, Physical and Engineering Sciences* 380 (10 2022). doi:10.1098/rsta.2021.0365.
- [32] Z. Wang, S. Das, A. Joshi, A. J. Shaikeea, V. S. Deshpande, 3d observations provide striking findings in rubber elasticity, *Proceedings of the National Academy of Sciences* 121 (24) (2024) e2404205121.
- [33] M. Mooney, A theory of large elastic deformation, *Journal of applied physics* 11 (9) (1940) 582–592.
- [34] R. S. Rivlin, Large elastic deformations of isotropic materials iv. further developments of the general theory, *Philosophical transactions of the royal society of London. Series A, Mathematical and physical sciences* 241 (835) (1948) 379–397.
- [35] R. S. Rivlin, Large elastic deformations of isotropic materials vi. further results in the theory of torsion, shear and flexure, *Philosophical Transactions of the Royal Society of London. Series A, Mathematical and Physical Sciences* 242 (845) (1949) 173–195.
- [36] R. S. Rivlin, D. Saunders, Large elastic deformations of isotropic materials vii. experiments on the deformation of rubber, *Philosophical Transactions of the Royal Society of London. Series A, Mathematical and Physical Sciences* 243 (865) (1951) 251–288.
- [37] R. W. Ogden, Large deformation isotropic elasticity—on the correlation of theory and experiment for incompressible rubberlike solids, *Proceedings of the Royal Society of London. A. Mathematical and Physical Sciences* 326 (1567) (1972) 565–584.
- [38] A. Anssari-Benam, A generalisation of the pucci–sacchandi model of rubber elasticity, *International Journal of Non-Linear Mechanics* 158 (2024) 104578.
- [39] J. Martins, E. Pires, R. Salvado, P. Dinis, A numerical model of passive and active behavior of skeletal muscles, *Computer methods in applied mechanics and engineering* 151 (3-4) (1998) 419–433.
- [40] E. Peña, J. A. Peña, M. Doblaré, On the mullins effect and hysteresis of fibered biological materials: A comparison between continuous and discontinuous damage models, *International Journal of Solids and Structures* 46 (7-8) (2009) 1727–1735.
- [41] K. Volokh, Hyperelasticity with softening for modeling materials failure, *Journal of the Mechanics and Physics of Solids* 55 (10) (2007) 2237–2264.
- [42] A. Anssari-Benam, Continuous softening up to the onset of failure: A hyperelastic modelling approach with intrinsic softening for isotropic incompressible soft solids, *Mechanics Research Communications* 132 (2023) 104183.
- [43] K. Volokh, On modeling failure of rubber-like materials, *Mechanics Research Communications* 37 (8) (2010) 684–689.
- [44] E. Peña, Computational aspects of the numerical modelling of softening, damage and permanent set in soft biological tissues, *Computers & Structures* 130 (2014) 57–72.
- [45] E. Peña, Prediction of the softening and damage effects with permanent set in fibrous biological materials, *Journal of the Mechanics and Physics of Solids* 59 (9) (2011) 1808–1822.

- [46] K. Volokh, Prediction of arterial failure based on a microstructural bi-layer fiber–matrix model with softening, *Journal of Biomechanics* 41 (2) (2008) 447–453.
- [47] E. Peña, V. Alastrué, A. Laborda, M. Martínez, M. Doblaré, A constitutive formulation of vascular tissue mechanics including viscoelasticity and softening behaviour, *Journal of biomechanics* 43 (5) (2010) 984–989.
- [48] B. Calvo, E. Pena, P. Martins, T. Mascarenhas, M. Doblaré, R. N. Jorge, A. Ferreira, On modelling damage process in vaginal tissue, *Journal of Biomechanics* 42 (5) (2009) 642–651.
- [49] L. Mullins, Softening of rubber by deformation, *Rubber chemistry and technology* 42 (1) (1969) 339–362.
- [50] J. Harwood, L. Mullins, A. R. Payne, Stress softening in natural rubber vulcanizates. part ii. stress softening effects in pure gum and filler loaded rubbers, *Journal of Applied Polymer Science* 9 (9) (1965) 3011–3021.
- [51] E. Peña, P. Martins, T. Mascarenhas, R. N. Jorge, A. Ferreira, M. Doblaré, B. Calvo, Mechanical characterization of the softening behavior of human vaginal tissue, *Journal of the mechanical behavior of biomedical materials* 4 (3) (2011) 275–283.
- [52] A. Anssari-Benam, G. Saccomandi, Continuous softening as a state of hyperelasticity: Examples of application to the softening behavior of the brain tissue, *Journal of Biomechanical Engineering* 146 (9) (2024).
- [53] M. Munoz, J. Bea, J. Rodríguez, I. Ochoa, J. Grasa, A. P. del Palomar, P. Zaragoza, R. Osta, M. Doblaré, An experimental study of the mouse skin behaviour: damage and inelastic aspects, *Journal of biomechanics* 41 (1) (2008) 93–99.
- [54] V. Alastrué, E. Peña, M. Martínez, M. Doblaré, Experimental study and constitutive modelling of the passive mechanical properties of the ovine infrarenal vena cava tissue, *Journal of biomechanics* 41 (14) (2008) 3038–3045.
- [55] R. W. Ogden, D. G. Roxburgh, A pseudo-elastic model for the mullins effect in filled rubber, *Proceedings of the Royal Society of London. Series A: Mathematical, Physical and Engineering Sciences* 455 (1999) 2861–2877.
- [56] G. Chagnon, E. Verron, L. Gornet, G. Marckmann, P. Charrier, On the relevance of continuum damage mechanics as applied to the mullins effect in elastomers, *Journal of the Mechanics and Physics of Solids* 52 (7) (2004) 1627–1650.
- [57] G. A. Holzapfel, B. Fereidoonzhad, Modeling of damage in soft biological tissues, in: *Biomechanics of living organs*, Elsevier, 2017, pp. 101–123.
- [58] L. Kachanov, Time of rupture process under deep conditions, *Izv. Akad. Nauk SSSR* 8 (1958) 26.
- [59] I. Rabotnov, *Elements of hereditary solid mechanics*, (No Title) (1980).
- [60] J. Lemaitre, How to use damage mechanics, *Nuclear engineering and design* 80 (2) (1984) 233–245.
- [61] J. C. Simo, On a fully three-dimensional finite-strain viscoelastic damage model: formulation and computational aspects, *Computer methods in applied mechanics and engineering* 60 (2) (1987) 153–173.
- [62] M. E. Gurtin, E. C. Francis, Simple rate-independent model for damage, *Journal of Spacecraft and Rockets* 18 (3) (1981) 285–286.
- [63] G. Z. Voyiadjis, P. I. Kattan, Investigation of the damage variable basic issues in continuum damage and healing mechanics, *Mechanics Research Communications* 68 (2015) 89–94.
- [64] A. Keller, K. Hutter, On the thermodynamic consistency of the equivalence principle in continuum damage mechanics, *Journal of the Mechanics and Physics of Solids* 59 (5) (2011) 1115–1120.
- [65] H. Weisbecker, D. M. Pierce, P. Regitnig, G. A. Holzapfel, Layer-specific damage experiments and modeling of human thoracic and abdominal aortas with non-atherosclerotic intimal thickening, *Journal of the mechanical behavior of biomedical materials* 12 (2012) 93–106.

- [66] T. Schmidt, D. Balzani, G. A. Holzapfel, Statistical approach for a continuum description of damage evolution in soft collagenous tissues, *Computer Methods in Applied Mechanics and Engineering* 278 (2014) 41–61.
- [67] T. C. Gasser, An irreversible constitutive model for fibrous soft biological tissue: a 3-d microfiber approach with demonstrative application to abdominal aortic aneurysms, *Acta Biomaterialia* 7 (6) (2011) 2457–2466.
- [68] C. Miller, T. C. Gasser, A microstructurally motivated constitutive description of collagenous soft biological tissue towards the description of their non-linear and time-dependent properties, *Journal of the Mechanics and Physics of Solids* 154 (2021) 104500.
- [69] J. F. Rodríguez, F. Cacho, J. A. Bea, M. Doblare, A stochastic-structurally based three dimensional finite-strain damage model for fibrous soft tissue, *Journal of the Mechanics and Physics of Solids* 54 (4) (2006) 864–886.
- [70] J. F. Rodríguez, V. Alastrue, M. Doblare, Finite element implementation of a stochastic three dimensional finite-strain damage model for fibrous soft tissue, *Computer methods in applied mechanics and engineering* 197 (9-12) (2008) 946–958.
- [71] A. Hamedzadeh, T. C. Gasser, S. Federico, On the constitutive modelling of recruitment and damage of collagen fibres in soft biological tissues, *European Journal of Mechanics-A/Solids* 72 (2018) 483–496.
- [72] G. A. Holzapfel, R. W. Ogden, A damage model for collagen fibres with an application to collagenous soft tissues, *Proceedings of the Royal Society A* 476 (2236) (2020) 20190821.
- [73] J. Lu, X. He, F. Auricchio, A waviness-centered damage model for collagenous soft tissues, *Acta Biomaterialia* 195 (2025) 134–143.
- [74] R. Xiao, T.-T. Mai, K. Urayama, J. P. Gong, S. Qu, Micromechanical modeling of the multi-axial deformation behavior in double network hydrogels, *International Journal of Plasticity* 137 (2021) 102901.
- [75] T.-T. Mai, T. Matsuda, T. Nakajima, J. P. Gong, K. Urayama, Damage cross-effect and anisotropy in tough double network hydrogels revealed by biaxial stretching, *Soft matter* 15 (18) (2019) 3719–3732.
- [76] C. Miller, T. C. Gasser, A bottom-up approach to model collagen fiber damage and failure in soft biological tissues, *Journal of the Mechanics and Physics of Solids* 169 (2022) 105086.
- [77] R. Dargazany, M. Itskov, A network evolution model for the anisotropic Mullins effect in carbon black filled rubbers, *International Journal of Solids and Structures* 46 (16) (2009) 2967–2977.
- [78] H. Gao, P. Klein, Numerical simulation of crack growth in an isotropic solid with randomized internal cohesive bonds, *Journal of the Mechanics and Physics of Solids* 46 (2) (1998) 187–218.
- [79] H. Gao, Elastic waves in a hyperelastic solid near its plane-strain equibiaxial cohesive limit, *Philosophical magazine letters* 76 (5) (1997) 307–314.
- [80] M. Born, On the stability of crystal lattices. i, in: *Mathematical Proceedings of the Cambridge Philosophical Society*, Vol. 36, Cambridge University Press, 1940, pp. 160–172.
- [81] P. Klein, J. Foulk, E. Chen, S. Wimmer, H. Gao, Physics-based modeling of brittle fracture: cohesive formulations and the application of meshfree methods, *Theoretical and Applied Fracture Mechanics* 37 (1-3) (2001) 99–166.
- [82] K. Park, Potential-based fracture mechanics using cohesive zone and virtual internal bond modeling, University of Illinois at Urbana-Champaign, 2009.
- [83] K. Park, G. H. Paulino, J. R. Roesler, A unified potential-based cohesive model of mixed-mode fracture, *Journal of the Mechanics and Physics of Solids* 57 (6) (2009) 891–908.
- [84] K. Volokh, H. Gao, On the modified virtual internal bond method, *Journal of Applied mechanics* 72 (6) (2005) 969–971.

- [85] L. Liu, Y. Li, Predicting the mixed-mode i/ii spatial damage propagation along 3d-printed soft interfacial layer via a hyperelastic softening model, *Journal of the Mechanics and Physics of Solids* 116 (2018) 17–32.
- [86] B. Ji, H. Gao, Mechanical properties of nanostructure of biological materials, *Journal of the Mechanics and Physics of Solids* 52 (9) (2004) 1963–1990.
- [87] W. Sun, B. Yin, K. Liew, Damage-induced energy dissipation in artificial soft tissues, *Journal of the Mechanics and Physics of Solids* 194 (2025) 105933.
- [88] P. Klein, H. Gao, Crack nucleation and growth as strain localization in a virtual-bond continuum, *Engineering fracture mechanics* 61 (1) (1998) 21–48.
- [89] H. Gao, B. Ji, Modeling fracture in nanomaterials via a virtual internal bond method, *Engineering Fracture Mechanics* 70 (14) (2003) 1777–1791.
- [90] K. Volokh, K. Ramesh, An approach to multi-body interactions in a continuum-atomistic context: Application to analysis of tension instability in carbon nanotubes, *International Journal of Solids and Structures* 43 (25-26) (2006) 7609–7627.
- [91] G. Thiagarajan, K. J. Hsia, Y. Huang, Finite element implementation of virtual internal bond model for simulating crack behavior, *Engineering Fracture Mechanics* 71 (3) (2004) 401–423.
- [92] P. Zhang, P. Klein, Y. Huang, H. Gao, P. Wu, Numerical simulation of cohesive fracture by the virtual-internal-bond model, *Computer Modeling in Engineering and Sciences* 3 (2) (2002) 263–277.
- [93] K. Y. Volokh, Nonlinear elasticity for modeling fracture of isotropic brittle solids, *J. Appl. Mech.* 71 (1) (2004) 141–143.
- [94] A. Faye, Y. Lev, K. Volokh, The effect of local inertia around the crack-tip in dynamic fracture of soft materials, *Mechanics of Soft Materials* 1 (1) (2019) 4.
- [95] T. Q. Bui, H. T. Tran, A localized mass-field damage model with energy decomposition: Formulation and fe implementation, *Computer Methods in Applied Mechanics and Engineering* 387 (2021) 114134.
- [96] K. Y. Volokh, Modeling failure and fracture in soft biological tissues, in: *Solid (Bio) mechanics: Challenges of the Next Decade: A Book Dedicated to Professor Gerhard A. Holzapfel*, Springer, 2022, pp. 391–406.
- [97] K. Volokh, Constitutive model of human artery adventitia enhanced with a failure description, *Mechanics of Soft Materials* 1 (2019) 1–9.
- [98] K. Volokh, Cavitation instability as a trigger of aneurysm rupture, *Biomechanics and modeling in mechanobiology* 14 (5) (2015) 1071–1079.
- [99] K. Volokh, Cavitation instability in rubber, *International Journal of Applied Mechanics* 3 (02) (2011) 299–311.
- [100] K. Volokh, Modeling failure of soft anisotropic materials with application to arteries, *Journal of the mechanical behavior of biomedical materials* 4 (8) (2011) 1582–1594.
- [101] Y. Lev, A. Faye, K. Volokh, Thermoelastic deformation and failure of rubberlike materials, *Journal of the Mechanics and Physics of Solids* 122 (2019) 538–554.
- [102] M. Goswami, A. Dutta, R. Kulshreshtha, G. Vasilyev, E. Zussman, K. Volokh, Mechanics of physically cross-linked hydrogels: Experiments and theoretical modeling, *Macromolecules* 58 (9) (2025) 4478–4487.
- [103] W. Li, X. Y. Luo, An invariant-based damage model for human and animal skins, *Annals of biomedical engineering* 44 (10) (2016) 3109–3122.
- [104] W. Li, Constitutive laws with damage effect for the human great saphenous vein, *Journal of the Mechanical Behavior of Biomedical Materials* 81 (2018) 202–213.

- [105] V. Normand, D. L. Lootens, E. Amici, K. P. Plucknett, P. Aymard, New insight into agarose gel mechanical properties, *Biomacromolecules* 1 (4) (2000) 730–738.
- [106] R. K. A. Pasumarthy, H. Tippur, Mechanical and optical characterization of a tissue surrogate polymer gel, *Polymer Testing* 55 (2016) 219–229.
- [107] J. Tang, M. A. Tung, J. Lelievre, Y. Zeng, Stress-strain relationships for gellan gels in tension, compression and torsion, *Journal of Food Engineering* 31 (4) (1997) 511–529.
- [108] G. Z. Voyiadjis, A. Samadi-Dooki, Hyperelastic modeling of the human brain tissue: effects of no-slip boundary condition and compressibility on the uniaxial deformation, *Journal of the mechanical behavior of biomedical materials* 83 (2018) 63–78.
- [109] G. Zhang, T. F. Guo, X. Guo, S. Tang, M. Fleming, W. K. Liu, Fracture in tension–compression–asymmetry solids via phase field modeling, *Computer Methods in Applied Mechanics and Engineering* 357 (2019) 112573.
- [110] M. Latorre, E. De Rosa, F. J. Montáns, Understanding the need of the compression branch to characterize hyperelastic materials, *International Journal of Non-Linear Mechanics* 89 (2017) 14–24.
- [111] K. Valanis, R. F. Landel, The strain-energy function of a hyperelastic material in terms of the extension ratios, *Journal of Applied Physics* 38 (7) (1967) 2997–3002.
- [112] K. C. Valanis, The valanis–landel strain energy function elasticity of incompressible and compressible rubber-like materials, *International Journal of Solids and Structures* 238 (2022) 111271.
- [113] K. Upadhyay, G. Subhash, D. Spearot, Thermodynamics-based stability criteria for constitutive equations of isotropic hyperelastic solids, *Journal of the Mechanics and Physics of Solids* 124 (2019) 115–142.
- [114] K. Upadhyay, G. Subhash, D. Spearot, Hyperelastic constitutive modeling of hydrogels based on primary deformation modes and validation under 3d stress states, *International Journal of Engineering Science* 154 (9 2020). doi:10.1016/j.ijengsci.2020.103314.
- [115] R. W. Ogden, G. Saccomandi, I. Sgura, Fitting hyperelastic models to experimental data, *Computational Mechanics* 34 (6) (2004) 484–502.
- [116] M. Destrade, G. Saccomandi, I. Sgura, Methodical fitting for mathematical models of rubber-like materials, *Proceedings of the Royal Society A: Mathematical, Physical and Engineering Sciences* 473 (2198) (2017) 20160811.
- [117] S. Budday, G. Sommer, C. Birkl, C. Langkammer, J. Haybaeck, J. Kohnert, M. Bauer, F. Paulsen, P. Steinmann, E. Kuhl, et al., Mechanical characterization of human brain tissue, *Acta biomaterialia* 48 (2017) 319–340.
- [118] S. Budday, G. Sommer, J. Haybaeck, P. Steinmann, G. A. Holzapfel, E. Kuhl, Rheological characterization of human brain tissue, *Acta biomaterialia* 60 (2017) 315–329.
- [119] S. Ambartsumyan, Elasticity theory of different moduli, *Trans. RF Wu and YZ Zhang. China Railway, Beijing* (1986).
- [120] K. Volokh, Review of the energy limiters approach to modeling failure of rubber, *Rubber Chemistry and Technology* 86 (3) (2013) 470–487.
- [121] J. C. Criscione, J. D. Humphrey, A. S. Douglas, W. C. Hunter, An invariant basis for natural strain which yields orthogonal stress response terms in isotropic hyperelasticity, *Journal of the Mechanics and Physics of Solids* 48 (12) (2000) 2445–2465.
- [122] M. Chen, Y. Tan, B. Wang, General invariant representations of the constitutive equations for isotropic nonlinearly elastic materials, *International journal of solids and structures* 49 (2) (2012) 318–327.
- [123] P. Neff, B. Eidel, R. J. Martin, Geometry of logarithmic strain measures in solid mechanics, *Archive for Rational Mechanics and Analysis* 222 (2) (2016) 507–572.

- [124] A. K. Landauer, X. Li, C. Franck, D. L. Henann, Experimental characterization and hyperelastic constitutive modeling of open-cell elastomeric foams, *Journal of the Mechanics and Physics of Solids* 133 (2019) 103701.
- [125] D. Prasad, K. Kannan, An analysis driven construction of distortional-mode-dependent and hill-stable elastic potential with application to human brain tissue, *Journal of the Mechanics and Physics of Solids* 134 (2020) 103752.
- [126] R. J. Martin, I.-D. Ghiba, P. Neff, A non-ellipticity result, or the impossible taming of the logarithmic strain measure, *International Journal of Non-Linear Mechanics* 102 (2018) 147–158.
- [127] V. Kulwant, K. Arvind, D. Prasad, P. Sreejith, K. Mohankumar, K. Kannan, A semi-analytical inverse method to obtain the hyperelastic potential using experimental data, *Journal of the Mechanics and Physics of Solids* 181 (2023) 105431.
- [128] F. O. Falope, L. Lanzoni, A. M. Tarantino, Energetic exhaustiveness for the direct characterization of energy forms of hyperelastic isotropic materials, *Journal of the Mechanics and Physics of Solids* 193 (2024) 105885.
- [129] E. Bremer-Sai, J. Yang, A. McGhee, C. Franck, Ballistic and blast-relevant, high-rate material properties of physically and chemically crosslinked hydrogels, *Experimental Mechanics* 64 (4) (2024) 587–592.
- [130] V. Tutwiler, J. Singh, R. I. Litvinov, J. L. Bassani, P. K. Purohit, J. W. Weisel, Rupture of blood clots: Mechanics and pathophysiology, *Science advances* 6 (35) (2020) eabc0496.
- [131] T. Lu, Z. Wang, J. Tang, W. Zhang, T. Wang, A pseudo-elasticity theory to model the strain-softening behavior of tough hydrogels, *Journal of the Mechanics and Physics of Solids* 137 (2020) 103832.
- [132] J. Jones, C. Marques, Rigid polymer network models, *Journal de Physique* 51 (11) (1990) 1113–1127.
- [133] M. Ramzi, C. Rochas, J.-M. Guenet, Structure- properties relation for agarose thermoreversible gels in binary solvents, *Macromolecules* 31 (18) (1998) 6106–6111.
- [134] J.-M. Guenet, C. Rochas, Agarose sols and gels revisited, in: *Macromolecular symposia*, Vol. 242, Wiley Online Library, 2006, pp. 65–70.
- [135] G. A. Holzapfel, *Nonlinear solid mechanics: a continuum approach for engineering science* (2002).
- [136] J. S. Bergstrom, *Mechanics of solid polymers: theory and computational modeling*, William Andrew, 2015.
- [137] K. Li, G. A. Holzapfel, Multiscale modeling of fiber recruitment and damage with a discrete fiber dispersion method, *Journal of the Mechanics and Physics of Solids* 126 (2019) 226–244.
- [138] P. Myhravaruni, K. Volokh, On incompressibility constraint and crack direction in soft solids, *Journal of Applied Mechanics* 86 (10) (2019) 101004.
- [139] M. Doi, Gel dynamics, *Journal of the Physical Society of Japan* 78 (5) (2009) 052001.
- [140] R. S. Rivlin, A. G. Thomas, Rupture of rubber. i. characteristic energy for tearing, *Journal of polymer science* 10 (3) (1953) 291–318.
- [141] K. Y. Volokh, Multiscale modeling of material failure: From atomic bonds to elasticity with energy limiters, *International Journal for Multiscale Computational Engineering* 6 (5) (2008).
- [142] P. Trapper, K. Y. Volokh, Elasticity with energy limiters for modeling dynamic failure propagation, *International Journal of Solids and Structures* 47 (2010) 3389–3396. doi:10.1016/j.ijsolstr.2010.08.016.
- [143] K. Volokh, New approaches to modeling failure and fracture of rubberlike materials, *Fatigue Crack Growth in Rubber Materials: Experiments and Modelling* (2021) 131–151.

- [144] A. D. Freed, Natural strain, *Journal of Engineering Materials and Technology* 117 (4) (1995) 379–385.
- [145] H. Hencky, The law of elasticity for isotropic and quasi-isotropic substances by finite deformations, *Journal of Rheology* 2 (2) (1931) 169–176.
- [146] J. C. Criscione, Direct tensor expression for natural strain and fast, accurate approximation, *Computers & structures* 80 (25) (2002) 1895–1905.
- [147] P. Flory, Thermodynamic relations for high elastic materials, *Transactions of the Faraday Society* 57 (1961) 829–838.
- [148] P. Neff, I.-D. Ghiba, J. Lankeit, The exponentiated hencky-logarithmic strain energy. part i: Constitutive issues and rank-one convexity, *Journal of Elasticity* 121 (2) (2015) 143–234.
- [149] J. Diani, P. Gilormini, Combining the logarithmic strain and the full-network model for a better understanding of the hyperelastic behavior of rubber-like materials, *Journal of the Mechanics and Physics of Solids* 53 (11) (2005) 2579–2596.
- [150] M. Baker, J. Ericksen, Inequalities restricting the form of the stress-deformation relations for isotropic elastic solids and reiner-rivlin fluids, *Journal of the Washington Academy of Sciences* 44 (2) (1954) 33–35.
- [151] D. Prasad, P. Sreejith, K. Kannan, A new viscoelastic model for human brain tissue using lode invariants based rate-type thermodynamic framework, *Applications in Engineering Science* 15 (2023) 100130.
- [152] L. G. Treloar, *The physics of rubber elasticity* (1975).
- [153] L. R. G. Treloar, The elasticity of a network of long-chain molecules. i, *Transactions of the Faraday Society* 39 (1943) 36–41.
- [154] L. R. Treloar, The elasticity of a network of long-chain molecules—ii, *Transactions of the Faraday Society* 39 (1943) 241–246.
- [155] P. J. Flory, J. Rehner Jr, Statistical mechanics of cross-linked polymer networks ii. swelling, *The journal of chemical physics* 11 (11) (1943) 521–526.
- [156] P. J. Flory, Network structure and the elastic properties of vulcanized rubber., *Chemical reviews* 35 (1) (1944) 51–75.
- [157] J. Steck, J. Kim, Y. Kutsovsky, Z. Suo, Multiscale stress deconcentration amplifies fatigue resistance of rubber, *Nature* 624 (7991) (2023) 303–308.
- [158] J.-Y. Sun, X. Zhao, W. R. Illeperuma, O. Chaudhuri, K. H. Oh, D. J. Mooney, J. J. Vlassak, Z. Suo, Highly stretchable and tough hydrogels, *Nature* 489 (7414) (2012) 133–136.
- [159] M. Islam, R. Picu, Effect of network architecture on the mechanical behavior of random fiber networks, *Journal of Applied Mechanics* 85 (8) (2018) 081011.
- [160] N. Filla, J. Hou, H. Li, X. Wang, A multiscale framework for modeling fibrin fiber networks: Theory development and validation, *Journal of the Mechanics and Physics of Solids* 179 (2023) 105392.
- [161] X. Liang, I. Chernysh, P. K. Purohit, J. W. Weisel, Phase transitions during compression and decompression of clots from platelet-poor plasma, platelet-rich plasma and whole blood, *Acta biomaterialia* 60 (2017) 275–290.
- [162] R. Long, C.-Y. Hui, Crack buckling in soft gels under compression, *Acta Mechanica Sinica* 28 (2012) 1098–1105.
- [163] C. Sun, P. K. Purohit, Rheology of fibrous gels under compression, *Extreme Mechanics Letters* 54 (2022) 101757.
- [164] A. Ed-Daoui, P. Snabre, Poroviscoelasticity and compression-softening of agarose hydrogels, *Rheologica Acta* 60 (6) (2021) 327–351.

- [165] J. Yang, W. Illeperuma, Z. Suo, Inelasticity increases the critical strain for the onset of creases on hydrogels, *Extreme Mechanics Letters* 40 (2020) 100966.
- [166] K. Volokh, On irreversibility and dissipation in hyperelasticity with softening, *Journal of Applied Mechanics* 81 (7) (2014) 074501.
- [167] J. Yang, H. C. Cramer III, E. C. Bremer, S. Buyukozturk, Y. Yin, C. Franck, Mechanical characterization of agarose hydrogels and their inherent dynamic instabilities at ballistic to ultra-high strain-rates via inertial microcavitation, *Extreme Mechanics Letters* 51 (2022) 101572.
- [168] K. Upadhyay, D. Spearot, G. Subhash, Validated tensile characterization of the strain rate dependence in soft materials, *International Journal of Impact Engineering* 156 (2021) 103949.
- [169] M. E. Wale, D. Q. Nesbitt, B. S. Henderson, C. K. Fitzpatrick, J. J. Creechley, T. J. Lujan, Applying astm standards to tensile tests of musculoskeletal soft tissue: Methods to reduce grip failures and promote reproducibility, *Journal of Biomechanical Engineering* 143 (1) (2021) 011011.
- [170] H.-J. Kwon, A. D. Rogalsky, C. Kovalchick, G. Ravichandran, Application of digital image correlation method to biogel, *Polymer Engineering & Science* 50 (8) (2010) 1585–1593.
- [171] G. Subhash, Q. Liu, D. Moore, P. Ifju, M. Haile, Concentration dependence of tensile behavior in agarose gel using digital image correlation, *Experimental Mechanics* 51 (2) (2011) 255–262.
- [172] R. Brown, *Physical testing of rubber*, Springer Science & Business Media, 2006.
- [173] D. Moreira, L. Nunes, Comparison of simple and pure shear for an incompressible isotropic hyperelastic material under large deformation, *Polymer Testing* 32 (2) (2013) 240–248.
- [174] O. Yeoh, Analysis of deformation and fracture of ‘pure shear’rubber testpiece, *Plastics, rubber and composites* 30 (8) (2001) 389–397.
- [175] M. Sutton, J. Yan, V. Tiwari, H. Schreier, J. Orteu, The effect of out-of-plane motion on 2D and 3D digital image correlation measurements, *Optics and Lasers in Engineering* 46 (10) (2008) 746–757. doi:10.1016/j.optlaseng.2008.05.005.
- [176] K. Upadhyay, G. Subhash, D. Spearot, Visco-hyperelastic constitutive modeling of strain rate sensitive soft materials, *Journal of the Mechanics and Physics of Solids* 135 (2020) 103777.
- [177] T. Sendova, J. R. Walton, On strong ellipticity for isotropic hyperelastic materials based upon logarithmic strain, *International Journal of Non-Linear Mechanics* 40 (2-3) (2005) 195–212.
- [178] K. Dušek, A. Choukourov, M. Dušková-Smrčková, H. Biederman, Constrained swelling of polymer networks: characterization of vapor-deposited cross-linked polymer thin films, *Macromolecules* 47 (13) (2014) 4417–4427.
- [179] I. Jayawardena, P. Turunen, B. C. Garms, A. Rowan, S. Corrie, L. Grøndahl, Evaluation of techniques used for visualisation of hydrogel morphology and determination of pore size distributions, *Materials Advances* 4 (2) (2023) 669–682.
- [180] M. Ghebremedhin, S. Seiffert, T. A. Vilgis, Physics of agarose fluid gels: Rheological properties and microstructure, *Current Research in Food Science* 4 (2021) 436–448.
- [181] K. Bertula, L. Martikainen, P. Munne, S. Hietala, J. Klefström, O. Ikkala, Nonappa, Strain-stiffening of agarose gels, *ACS Macro Letters* 8 (6) (2019) 670–675.
- [182] L. M. Barrangou, C. R. Daubert, E. A. Foegeding, Textural properties of agarose gels. i. rheological and fracture properties, *Food hydrocolloids* 20 (2-3) (2006) 184–195.
- [183] R. W. Ogden, *Non-linear elastic deformations*, Courier Corporation, 1997.
- [184] J. M. Ball, Convexity conditions and existence theorems in nonlinear elasticity, *Archive for rational mechanics and Analysis* 63 (4) (1976) 337–403.
- [185] R. Hill, On uniqueness and stability in the theory of finite elastic strain, *Journal of the Mechanics and Physics of Solids* 5 (4) (1957) 229–241.

- [186] R. Hill, On constitutive inequalities for simple materials—i, *Journal of the Mechanics and Physics of Solids* 16 (4) (1968) 229–242.
- [187] S. Hartmann, P. Neff, Polyconvexity of generalized polynomial-type hyperelastic strain energy functions for near-incompressibility, *International journal of solids and structures* 40 (11) (2003) 2767–2791.
- [188] G. Kissas, S. Mishra, E. Chatzi, L. De Lorenzis, The language of hyperelastic materials, *Computer Methods in Applied Mechanics and Engineering* 428 (2024) 117053.
- [189] Y. Dormoy, S. Candau, Transient electric birefringence study of highly dilute agarose solutions, *Biopolymers: Original Research on Biomolecules* 31 (1) (1991) 109–117.
- [190] T. Fujii, T. Yano, H. Kumagai, O. Miyawaki, Scaling analysis on elasticity of agarose gel near the sol–gel transition temperature, *Food hydrocolloids* 14 (4) (2000) 359–363.
- [191] H. Dal, K. Açıkgöz, Y. Badienia, On the performance of isotropic hyperelastic constitutive models for rubber-like materials: a state of the art review, *Applied Mechanics Reviews* 73 (2) (2021) 020802.
- [192] J. Guan, X. Li, H. Yuan, J. Liu, Hyperelastic modeling based on generalized landau invariants and multi-stage calibration, *Journal of the Mechanics and Physics of Solids* (2025) 106338.
- [193] Y. Xiang, D. Zhong, P. Wang, G. Mao, H. Yu, S. Qu, A general constitutive model of soft elastomers, *Journal of the Mechanics and Physics of Solids* 117 (2018) 110–122.
- [194] F. Pervin, W. W. Chen, Mechanically similar gel simulants for brain tissues, in: *Dynamic Behavior of Materials, Volume 1: Proceedings of the 2010 Annual Conference on Experimental and Applied Mechanics*, Springer, 2011, pp. 9–13.
- [195] Y. Hong, M. Sarntinoranont, G. Subhash, S. Canchi, M. King, Localized tissue surrogate deformation due to controlled single bubble cavitation, *Experimental Mechanics* 56 (1) (2016) 97–109.
- [196] S. Aghayan, K. Weinberg, Experimental and numerical investigation of dynamic cavitation in agarose gel as a soft tissue simulant, *Mechanics of Materials* 175 (2022) 104486.
- [197] P. Mythravaruni, K. Volokh, Failure of rubber bearings under combined shear and compression, *Journal of Applied Mechanics* 85 (7) (2018).
- [198] D. Millar, M. Mennu, K. Upadhyay, C. Morley, P. Ifju, An improved direct shear characterisation technique for soft gelatinous and elastomeric materials, *Strain* 57 (3) (2021) e12383.
- [199] J. T. Cantrell, S. Rohde, D. Damiani, R. Gurnani, L. DiSandro, J. Anton, A. Young, A. Jerez, D. Steinbach, C. Kroese, et al., Experimental characterization of the mechanical properties of 3d-printed abs and polycarbonate parts, *Rapid Prototyping Journal* 23 (4) (2017) 811–824.

A constitutive framework for tension–compression failure asymmetry in soft materials

Yogesh C. Chandrashekar, Kshitiz Upadhyay*

*Department of Aerospace Engineering and Mechanics, University of Minnesota,
Minneapolis, MN 55455, USA*

Supplementary Material

S.1 Influence of softening sharpness parameters on the stress–reduction behavior

This section provides supplementary context for the evolution of the stress–reduction factor $\text{Red}(\lambda)$ with softening sharpness parameters m^\pm , discussed in Section 6.1 of the main manuscript. Both the failure parameters (Φ^\pm, m^\pm) govern the decay of the intact hyperelastic response via the mode-specific reduction factor prior to rupture. To illustrate the qualitative role of m^\pm , we examine the stress–reduction factor $\text{Red}(\lambda) = \exp\left[-\left(\frac{W(\lambda)}{\Phi^\pm}\right)^{m^\pm}\right]$, for representative tensile (m^+) and compressive (m^-) softening sharpness parameters while holding the corresponding pseudo–failure energies (Φ^\pm) fixed.

For this illustration, we consider the mode-specific pseudo–failure energies (Φ^\pm) from the calibrated values of a representative 3% w/v agarose specimen using the proposed asymmetric failure model reported in the main manuscript: $\Phi^+ = 3.97$ kPa and $\Phi^- = 14.49$ kPa. With these values fixed, the softening sharpness parameters are varied as follows: $m^+ \in \{2, 5, 50\}$ and $m^- \in \{0.2, 0.4, 0.8\}$.

Figure S.1 shows the resulting stress–reduction trajectories $\text{Red}(\lambda)$ in tension ($\lambda > 1$) and compression ($\lambda < 1$). These curves illustrate how

*Corresponding author. Email: kshitizu@umn.edu

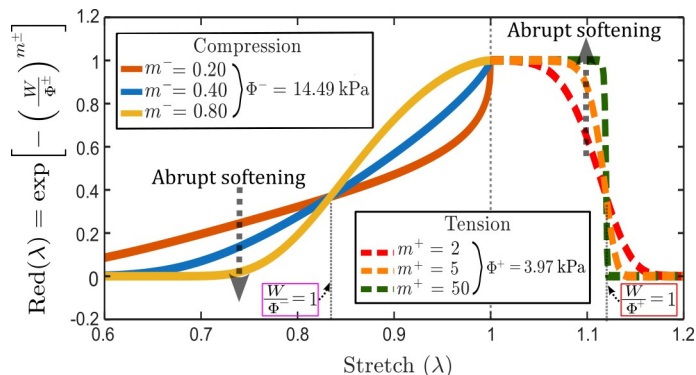


Figure S.1: Representative stress–reduction curves in tension and compression for selected values of the softening sharpness parameters $m^+ \in \{2, 5, 50\}$ and $m^- \in \{0.2, 0.4, 0.8\}$, using fixed mode-specific pseudo–failure energies $\Phi^+ = 3.97$ kPa and $\Phi^- = 14.49$ kPa corresponding to the calibrated parameters of a 3% w/v agarose specimen using the proposed asymmetric failure model. These curves provide a conceptual illustration of the behavior of the stress–reduction factor $\text{Red}(\lambda)$ discussed in Section 6.1 of the main manuscript.

the softening sharpness parameters m^\pm govern the steepness of the reduction profile as the stored energy $W(\lambda)$ approaches the corresponding mode-specific pseudo–failure thresholds Φ^\pm . For fixed Φ^\pm , variations in m^\pm determine whether the onset and progression of softening occur gradually or abruptly, thereby highlighting the distinct tensile and compressive softening behaviors encoded within the proposed asymmetric–failure formulation.

The influence of the compressive softening parameter m^- , when $m^- < 1$, is more nuanced, since the $\text{Red}(\lambda)$ depends significantly on both the normalized stored energy $W(\lambda)/\Phi^-$ and m^- . In the small-stretch regime, where $W(\lambda)/\Phi^- < 1$, a smaller m^- yields a larger value of $(W(\lambda)/\Phi^-)^{m^-}$, causing $\text{Red}(\lambda)$ to deviate from unity earlier in the loading history. Consequently, softening activates at relatively smaller compressive stretches.

As compression progresses and $W(\lambda)/\Phi^-$ exceeds unity (see the figure), this ordering reverses: a larger m^- amplifies the term $(W(\lambda)/\Phi^-)^{m^-}$, leading to a steeper decline in the $\text{Red}(\lambda)$ as damage propagates. This crossover behavior, evident in Fig. S.1 near $\lambda \approx 0.83$ (where $W(\lambda)/\Phi^- = 1$), explains why the curve with the smallest m^- departs earliest from unity, while the curve with the largest m^- exhibits the most abrupt decay at larger compressive strains.

In contrast, the tensile branch, where $m^+ \gg 1$, the abruptness of failure

exhibits a monotonic dependence on m^+ regardless of the applied stretch value: increasing m^+ keeps $\text{Red}(\lambda)$ close to unity over most of the deformation path and then produces an increasingly abrupt drop to zero as it approaches the tensile failure threshold. Together, these behaviors mirror the asymmetric softening patterns discussed in Section 6.1 of the main manuscript and highlight the distinct mechanisms governing tensile and compressive failure in agarose gels.